Physics of black hole formation in failed supernovae

by

Mario G. Ivanov

A thesis submitted in partial fulfillment of the requirements for the degree of

Master of Science

Department of Physics
University of Alberta

Abstract

I present the formation and evolution of the shock wave driven by neutrino losses in failed core-collapse supernovae that form black holes (BHs). Neutrino losses result in a decrease in the gravitational mass, which leads to the formation of an outward shock. The ejected mass and energy vary widely depending on the classification of the progenitor and the equation of state (EOS) of dense matter. Simulating the inner regions of stellar core-collapse, where the energetics of this phenomenon are set, demands a general-relativistic (GR) neutrino radiation hydrodynamic approach. Publicly available codes do not have a large enough dynamic range to simultaneously model the outer stellar regions, where mass ejection occurs, and the inner core. Previous work on this problem has parameterized the evolution of the inner core, treating it as an effective point mass below a cut-off radius. Here we improve this method by simulating the inner core with a time-dependent, spherically symmetric neutrino radiation hydrodynamics code and the outer layers with a Newtonian code that covers the relevant dynamic range. We use the detailed neutrino mass-loss history in the inner core to modify the gravitational mass felt by the outer layers, that ultimately eject mass. We report several results: (i) we find that the ejecta mass and energy can vary by a factor of several depending on

the EOS used, with a stiff EOS matching previous parametric results and a softer EOS leading to less ejected mass and lower energies; (ii) red and yellow supergiant stars have energetically bound ejecta when not including hydrogen recombination energy; (iii) increasing the spatial resolution led to converging results for Wolf-Rayet stars; and (iv) we quantitatively, but not qualitatively, modify previous observational predictions.

Preface

This thesis is an original work by Mario G. Ivanov. The topic of this thesis is a continuation study of work done in 2018 by Dr. Fernández and collaborators. I ran simulations, made modifications to the code, and fixed bugs to allow the code to simulate different neutrino mass loss prescriptions and the ability to remap the domain and the evolution of the gravitational mass from `GR1D`. I performed post processing using my own scripts, which built on previous scripts provided by Dr. Fernández. I wrote the first working draft of our journal article manuscript and made all figures included in this thesis. This manuscript (in preparation) has been heavily edited by Dr. Fernández and myself, and Chapters 2 and 3 borrow substantial content from it. I fully wrote the remaining chapters, with only minor corrections made by Dr. Fernández.

During my M.Sc., I also worked on a couple of other projects not included in this thesis. The first was an exploratory study of globular clusters, open clusters, and galaxies with Dr. Craig Heinke, which was published in the Monthly Notices of the Royal Astronomical Society Journal as Heinke C.O., M. G. Ivanov, et al. 2020, "The X-ray emissivity of low-density stellar populations", MNRAS, 492, 4, March 2020, 5684-5708. The second is a project that I am still working on with Dr. Sivakoff and it involves developing a post-processing pipeline to analyze lightcurves and spectra obtained from the AstroSat telescope. We are currently working with data on the black hole X-ray binary GX339-4.

"I don't believe in astrology; I'm a Sagittarius and we're skeptical."

Arthur C. Clarke

Acknowledgements

I would like to thank the support, patience, and understanding of my two official co-supervisors, Rodrigo Fernández and Gregory Sivakoff, as well as Craig Heinke, with whom I published my first paper. I would also like to thank my office mates, Coleman Dean and Steven Fahlman, who often provided useful insights, funny remarks, and made coming in to work a joy. Lastly, I would like to thank my family and especially my wife, for trying their best to take interest in my work and in their support when I quit my dental career to follow my passion in astrophysics.

Nomenclature

BH	Black Hole
BSG	Blue Supergiant
ccSNe	Core-collapse Supernovae
EM	Electromagnetic
EOS	Equation of State
GR	General-Relativity
NS	Neutron Star
RSG	Red Supergiant
SN	Supernova
TOV	Tolman-Oppenheimer-Volkoff
WR	Wolf-Rayet
YSG	Yellow Supergiant
ZAMS	Zero-age Main Sequence

Contents

List of Tables

List of Figures

Chapter 1

Introduction

Massive stars, those with a zero-age main sequence (ZAMS) mass (M_{ZAMS}) in the range of $8 \lesssim M_{ZAMS}/M_{\odot} \lesssim 150$, are the progenitors of core-collapse supernovae (SNe). When a massive star is reaching the end of its life, it undergoes shell burning, where several different chemical layers are each fusing into heavier elements to fuel the star. While on the pathway to iron, the star is able to extract energy out of fusion to use in the battle against gravity. Unfortunately, fusing iron into heavier elements is an endothermic process. This means that the last exothermic step for any massive star is the fusion to iron. As the onion-like structure of shell burning continues to add iron to the core, this inert ash increasingly hinders the star's ability to combat gravity. The iron core continues to grow until it reaches its effective Chandrasekhar mass, after which the electron degeneracy pressure can no longer support the core and the core collapses.

As a result, a catastrophic explosion, so luminous that it can be seen across billions of light-years, forges a compact and massive remnant — either a neutron star (NS) or a BH. These bright transients are among some of the most important phenomena in astrophysics, not only because explosions are awesome, but also due to how energetic they are and the nucleosynthesis that occurs during the explosion.

The cores of isolated stars with ZAMS masses less than $8\,M_\odot$ will never get massive enough to collapse, so those stars eventually lose their envelope as a planetary nebula and become white dwarfs. Stars more massive than $\sim 140\,M_\odot$ explode via mechanisms known as pair instability and pulsational pair instability (see Kasen et al. 2011), where a remnant is not left behind. Any stars with ZAMS masses $\gtrsim 250\,M_\odot$ will form black holes immediately, because the explosive nuclear burning that occurs when a star of this mass collapses on itself is not energetic enough to resist the collapse. (Fryer et al., 2001)

The term "supernovae" was first used by Baade and Zwicky (1934a,b,c), where they hypothesized that the observed SN would release energy that would equal a substantial fraction of the star's rest mass and that the explosion may lead to a "transition of an ordinary star to a neutron star, consisting of mainly neutrons." It was a revolutionary prediction at that time. The nuclear processes that occurred in stars were not known, and yet this prediction still forms our basic understanding of stellar death and the birth of NSs today.

Modelling the behaviour of core-collapse and the resulting supernova proved to be no easy task. Even in one-dimension (1D), there is no single dominant force or set of equations that one could solve analytically and properly predict what would happen when any given progenitor star submits to gravity and experiences core-collapse. In essence, there are many competing processes that determine if a star undergoes a successful explosion (SN) or a failed explosion (BH) in a time frame of a matter of seconds.

It was with the work of Colgate and White (1966) that the scientific community was presented with the first numerical simulations of the hydrodynamic behaviour of supernovae. In their work, they found that the thermonuclear energy available from the gravitational collapse "undoubtedly occurs, but in [their] view it is too small to significantly affect the subsequent dynamical history of the star." This was an argument against another supernova idea at the

time that argued the core would bounce back from nuclear density and propagate into the mantle of the star. We now know that this mechanism does not work, because the bounce always stalls. Instead, Colgate and White (1966) argued that the dominant "transfer of energy takes place by the emission and deposition of neutrinos." Their idea was that the energy released during the gravitational collapse would bring the temperature of the core to $\sim 10^{11}\,\mathrm{K}$, which is equivalent to tens of MeV. With the amount of available energy, if even a small fraction, say $\sim 1\%$, of the neutrinos produced in the core and radiated away were to be reabsorbed back into the star, it could be enough energy to drive the explosion. This "delayed-shock" supernova idea was debated and criticised, but with gradually improved numerical schemes and increasingly higher computational power, Wilson (1985) and others developed it further, to the point where today it has become the main paradigm for explaining the explosions of core-collapse SNe (ccSNe).

Today, we are at a point in time when we have access to supercomputers and algorithms that allow us to study the hydrodynamics of ccSNe in more detail than ever before. The most state-of-the-art simulations evolve ccSNe from the onset of core-collapse through an intensely detailed explosion using advanced treatment of physics, like neutrino transport. Even then, given limitations in computational power, full-scale 3D models employ a variety of approximations: for example, assuming rapid rotation (Janka et al., 2016); nonstandard neutrino opacity calculations (Melson et al., 2015); or starting from spherically symmetric initial conditions rather than simulating the full 3D flow of matter in stars before core collapse, which perturbs the different advanced burning stages in high-mass stars. (Couch and Ott, 2015; Couch et al., 2015; Müller et al., 2016a,b)

Due to these complexities, scientists to this day still find interesting physics in simpler 1D and 2D simulations that can probe certain parameter spaces swiftly and with substantially more detail than previously possible. These new

patterns that emerge help us understand the broader picture in concert with the newest 3D simulations.

1.1 Overview of the explosion mechanism

The neutrino-driven explosion model proposed by Colgate and White (1966) is currently the main mechanism used for explaining most ccSNe. It has proved successful in reviving the SN for low-mass progenitors, stars in the 8–10 $M_\odot$ range that have an O-Ne-Mg core instead of an iron core, with observational properties such as energy and nucleosynthesis yields similar to prototypical SN such as the Crab SN. Even though there have been amazing advancements in the modelling of SN, for more massive progenitors that form iron cores, the main problem is that the 3D results are not robust. Sometimes these progenitors do not explode, even where asymmetries in 3D increase the likelihood of explosion; or when they explode, their explosion energies are lower than observations. So, the results for high-mass progenitors are uncertain on top of the fact that approximations must be used given computational limitations. While there are other proposed explosion mechanisms, like the magnetorotational mechanism, they cannot account for the majority of observed supernovae.

Following the description of Janka (2017), the supernova begins at core collapse. A gravitational instability causes material to fall inwards towards the core of the star. The accretion of this infalling material onto the core increases the central density dramatically to nuclear densities. A new stable inner core is formed due to the stiffening of the EOS, but the infalling material overshoots the new equilibrium, creating a pressure wave that steepens into a shock front radially outwards. The energy in the shock dissipates quickly, due to the photodissociation of iron and neutrino emission, and stalls well inside the iron core to form an accretion shock. While the shock is moving

outwards, the volume behind it is thermalized and made up of free nucleons. This allows for the accretion shock to be heated by the neutrinos emitted by the contracting and increasingly hotter nascent NS. If enough energy is transferred into the regions just inside the shock, it revives the supernova explosion. A positive feedback loop occurs where the more energy that is inputted into the shock, the more energy it has to move outwards and the more total volume it occupies. This in turn increases the total volume over which the shock can absorb more energy. The outward acceleration of the shock triggers explosive nucleosynthesis and leads to the unbinding of the stellar envelope by the shock — a supernova.

When a successful explosion occurs, what is left behind is a NS. However, there are a couple of pathways that can lead to the generation of a stellar-mass BH. The first is if the explosion is successful, but weak, there may be enough material ejected that is gravitationally bound that would eventually accrete back onto the NS to push it over the maximum mass that can be supported by the nuclear EOS. This is referred to as a "fallback supernova." The second is where the supernova mechanism fails to revive the explosion at the accretion shock stage and the protoneutron star collapses in on itself. The existence of such "unnovae" (Kochanek et al., 2008) are the focus of my thesis.

1.2 The Failures

Studying the outcome of failing supernovae is particularly interesting. We get to study the formation of BHs, a current hot topic in astrophysics due to the recent detection of gravitational waves from binary BHs by Advanced LIGO and Virgo. We also get to explore the failed SNe cases that we now know could give off detectable electromagnetic (EM) signals.

If the progenitor has sufficient rotation for an accretion disk to form around the BH, outflows from this disk and/or a relativistic jet can power a supernova

and possibly also a long gamma-ray burst (MacFadyen and Woosley, 1999).

For the case of dynamically unimportant rotation, Nadyozhin (1980) was the first to put forth the idea that a failed SN may still have an EM signature. When the supernova mechanism fails to revive the accretion shock, the star is doomed to collapse on itself and form a BH. However, neutrinos emitted by the forming NS carry a significant amount of energy away, enough to cause a shift in the gravitational potential for the outer stellar layers. The hydrodynamic response of the star to an abrupt change in the gravitational mass causes another shock, different from the accretion shock mentioned earlier and more akin to a sound pulse, to make its way through the star. This shock, if energetic enough, can be ejected from the star with energies large enough to potentially be detected. This thesis is an extension of this idea.

One particular controversy over the past decade kept scientists interested in this topic. Even before the detection of gravitational waves, scientists found an apparent lack of high mass SN progenitors that ought to be red supergiants. Kochanek et al. (2008) proposed a survey to find failed supernovae by tracking a million supergiants and looking for disappearances. The survey began, but just about a year later, Smartt et al. (2009) found that the (at the time) known Type II-P SN progenitors had an upper mass limit of $\sim 18\,\mathrm{M}_\odot$. However, progenitors with masses up to $\sim 25\,\mathrm{M}_\odot$ are known to evolve as red supergiants (RSG) and explode. This discrepancy became well-known in the literature as the "Red Supergiant Problem." Many papers came out to try and explain this apparent gap with different physical treatments in their stellar evolution codes, including arguments about the errors and trustworthiness of these codes, though none had a smoking gun explanation.

In the numerical calculations from Lovegrove and Woosley (2013), who simulated a failed supernova in a $15\,\mathrm{M}_\odot$ and a $25\,\mathrm{M}_\odot$ RSG, they found that the resultant ejected material could have a luminosity on the order of $\sim 10^{39}\,\mathrm{erg\,s^{-1}}$ for about a year, which the survey proposed by Kochanek et al. (2008) should

be able to observe as a sudden brightening of the "star" followed by a gradual disappearance. The bulk of the energy in the shock was calculated from hydrogen recombination. It was also in this year that Piro (2013) published predictions for a much brighter ($L_{peak} \sim 10^{40} - 10^{41}\,erg\,s^{-1}$) optical transient that would last $\sim$3–10 days as the shock breaks out of the stellar photosphere. At this point, the physics of black hole formation became much more interesting and complex as there could be mass ejected that could provide us both a window into how exactly the black hole was formed and as a prediction for observations.

The prediction brought about excitement as the first update from the proposed survey (Gerke et al., 2015) was published with 4 years of survey data, including the first detected disappearance of a star, credited as a failed supernova candidate. The progenitor was found to have an estimated mass of 18–25 $M_\odot$, right in the range of the Red Supergiant Problem, and a stable luminosity for two of their epochs followed by a sudden outburst before it disappeared. This study also provided us with a new important parameter that would later become a focus of many other works — the fraction of failed SNe compared to all SNe. If this candidate was indeed a failed SN, the fraction was calculated to be $0.07 \leq f \leq 0.62$ at 95% confidence.

Adams et al. (2017) provided more evidence that the candidate found in Gerke et al. (2015) was a failed SN, after analyzing archival imaging of the progenitor in 2009. The progenitor spectral energy distribution was fit well with a $\sim 25\,M_\odot$ RSG and most importantly, had a weak ($\sim 10^6\,L_\odot$) and long (3–11 month) optical outburst that was roughly consistent with the work of Lovegrove and Woosley (2013). The survey also reconfirmed their hypothesis in Basinger et al. (2020) to rule out some other theories and arguments regarding this failed SN candidate.

More recently, Fernández et al. (2018) (hereafter F18) explored the properties of the neutrino mass-energy loss mechanism over a range of progenitors

with numerical simulations. They found that most progenitor types (not just RSGs) could eject mass, opening up the possibility for an even broader range of observable signatures of failed SNe. Their ejected mass for RSGs ($\sim M_\odot$) was qualitatively similar to those of Lovegrove and Woosley (2013), and they reported shock breakout luminosities ($\sim 10^{40}\,\mathrm{erg\,s^{-1}}$) that agree with those of Piro (2013) and total kinetic energies ($\sim 10^{47}\,\mathrm{erg}$) that agree with Lovegrove et al. (2017). Ejecta properties for other stellar types have very different values than for RSGs.

My work follows the work of F18 by improving the simulations of the range of progenitors in several ways. The main addition of my work is the new treatment of the evolution of the inner core of the stars. The general-relativistic hydrodynamics code `GR1D` was used to model the inner star, while continuing to use the Newtonian code `FLASH` to model the hydrodynamic response of the rest of the star. We use `GR1D` to simulate the full, detailed history of neutrino emission from the inner core, rather than using an analytic prescription. This gives a physically grounded value for the gravitational mass lost to neutrinos, with a dependence on the EOS of dense matter, in contrast to the parameterized treatment used in F18. We also vary the EOSs used because they are an uncertain input into the `GR1D` calculations. Testing a range of them allows us to quantify the degree of uncertainty when using any given EOS. The spatial resolution of the simulations was also increased enough to properly resolve the surface pressure scale height of all fiducial progenitors. This has implications for shock breakout predictions.

Chapter 2

Methods

2.1 Physical Model and Approximations

Our aim is to compute the hydrodynamic response of a collapsing massive star to the decrease in the gravitational mass from neutrino emission after core bounce in the case where the supernova fails and a black hole forms. We restrict ourselves to progenitors for which rotation is negligible and we ignore the effect of hydrodynamic instabilities that operate within the first seconds after bounce, both of which have an important role in a successful explosion (here we only consider failures). We therefore carry out our analysis in spherical symmetry. We also ignore any circumstellar material that the star could have ejected prior to undergoing core-collapse. This material can modify the observational signatures of shock breakout (e.g., Katz et al. 2012; Haynie and Piro 2020). Our focus is the total energy and mass of any ejecta arising from the change in gravitational acceleration.

In the previous work by F18, the inner stellar core was removed and the hydrodynamic response of the star was computed using analytic prescriptions for the evolution of the gravitational mass enclosed within this radius. This removal was done to avoid a restrictive hydrodynamic time step in regions approaching the origin. The enclosed mass evolves due to material accreted

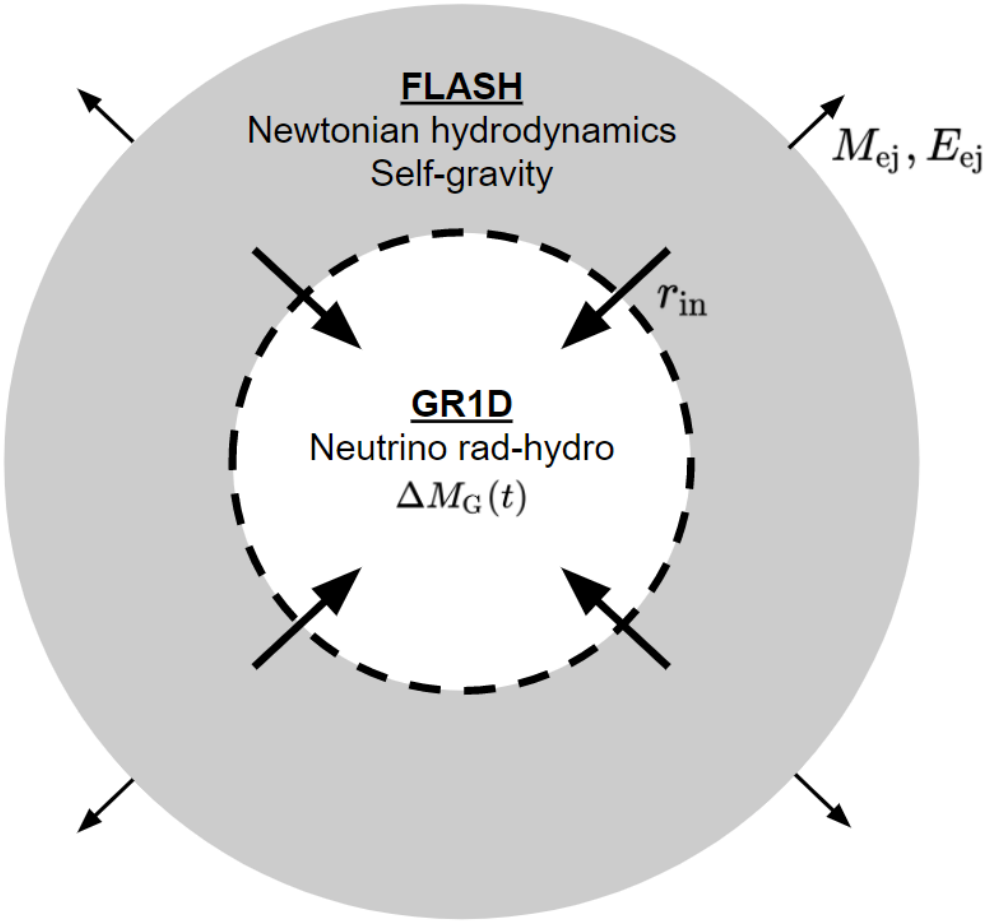

Figure 2.1: Schematic of our computational approach. For a given presupernova progenitor (Section 2.2) and dense-matter EOS, the evolution of the inner core is followed with the general-relativistic, neutrino radiation-hydrodynamics code `GR1D` (Section 2.3), focusing on the gravitational mass lost to neutrinos $\Delta M_{\rm G}(t)$ (Equation 2.9) at some transition radius $r_{\rm in}$. The region outside $r_{\rm in}$ is then evolved with `FLASH`, accounting for the mass flowing supersonically into $r_{\rm in}$ as well as the change in gravity due to $\Delta M_{\rm G}(t)$ (Section 2.4), and focusing on any mass ejected from the stellar surface. The majority of our models only interpolate $\Delta M_{\rm G}(t)$ from `GR1D`, while a smaller sample employs an analytic approximation for this function or maps the initial condition for `FLASH` directly from `GR1D` (Table 2.2).

through the inner radius and due to neutrino emission during the PNS phase (see also Lovegrove and Woosley 2013). This modeling approach is acceptable because material that accretes through the inner boundary reaches supersonic speeds shortly after collapse, without any hydrodynamic feedback on the outer layers.

Here we replace the analytic prescriptions for the inner core evolution used in F18 with a spherically-symmetric neutrino radiation-hydrodynamic calculation. Due to the complexity of the latter and the limitations in thermodynamic range set by publicly available EOSs of nuclear matter, we can carry out this calculation self-consistently only until a BH forms, and within a limited volume inside the star. Nevertheless, the supersonic character of matter infall and the rapidly increasing dynamical time with stellar radius allow for a decoupling in the modeling of the inner core and the outer layers of the star with separate codes (there is overlap, but I explain that later when discussing remap mode) for each regime, without a significant loss in consistency.

2.2 Pre-supernova progenitors

The pre-supernova stars we explore are shown in Table 2.1. We adopt the same fiducial solar-metallicity progenitors as in F18: a $15\,M_\odot$ RSG, a $25\,M_\odot$ blue supergiant (BSG), and a $40\,M_\odot$ Wolf-Rayet star (WR). These three progenitors represent three different cases for the evolution of the stellar envelope: the RSG stars have a convective hydrogen envelope; the BSG stars have a radiative envelope; and the WR stars have such strong stellar winds and lose mass at such a high rate that their envelope is stripped away to reveal their helium cores. These models also cover three different regimes of the core compactness parameter (O'Connor and Ott, 2011; Sukhbold and Woosley, 2014)

$$\xi_{2.5} = \frac{2.5}{r(M = 2.5\,M_\odot)/1000\text{ km}}, \tag{2.1}$$

where $r(M = 2.5\,M_\odot)$ stands for the radial coordinate that encloses $2.5\,\mathrm{M}_\odot$ (it is chosen by convection), and in envelope compactness

$$\xi_{\rm env} = \frac{(M_{\rm cc}/M_\odot)}{(R_{\rm cc}/R_\odot)}, \tag{2.2}$$

where $M_{\rm cc}$ and $R_{\rm cc}$ are the mass and radius of the star at core-collapse. The core compactness of stars, which is a measure of the amount of mass contained within a given radius and hence of the strength of the gravitational potential, has been previously used in determining the success or failure of ccSNe simulations. We therefore use it as a connection to previous works (O'Connor and Ott, 2011; Ugliano et al., 2012; Ertl et al., 2016). The encompassing mass for $\xi_{2.5}$ was chosen to be $2.5\ \mathrm{M}_\odot$ as it relates to the maximum NS mass, and thus has a correlation with black hole formation. The values of $\xi_{2.5}$ and $\xi_{\rm env}$ are shown in Table 2.1. In addition to these baseline models, R15, B25, and W40, we consider two yellow supergiants (YSGs) — one of solar metallicity (Y22) and another of low-metallicity (Y25) — a massive low-metallicity blue supergiant (B80), and a $50\,\mathrm{M}_\odot$ solar-metallicity WR star (W50). The YSGs are selected such than one of the compactness parameters, either $\xi_{2.5}$ or $\xi_{\rm env}$, has a value similar to R15, while the other varies. W50 has a higher core-compactness than W40, and B80 has high values of both core- and envelope compactness (in F18 no mass is ejected from this model). All of these progenitors are computed with the stellar evolution code `MESA` version 6794 (Paxton et al., 2011, 2013, 2015, 2018, 2019). Parameters and physical choices are described in Fernández et al. (2018), and inlists, the files used by `MESA` to generate the stars used in this research, are publicly available[1].

To connect with previous work, we also evolve models s20 and s40 from

[1] `bitbucket.org/rafernan/bhsn_mesa_progenitors`

Table 2.1: Presupernova progenitors used in this study. Columns from left to right show model name, type of star (RSG: red supergiant; YSG: yellow supergiant; BSG: blue supergiant; and WR: Wolf-Rayet), zero-age main sequence mass, metallicity, mass at core-collapse, effective temperature at core-collapse, core compactness (eq. [2.1]), and envelope compactness (eq. [2.2]). The fiducial models are the first three listed.

Model	Type	M_{zams} ($M_\odot$)	Z ($Z_\odot$)	M_{cc} ($M_\odot$)	T_{eff} (10^3 K)	$\xi_{2.5}$	ξ_{env}
R15	RSG	15	1.00	11	3	0.24	0.010
B25	BSG	25	1.00	12	15	0.33	0.120
W40	WR	40	1.00	10	260	0.37	27
Y22	YSG	22	1.00	11	5	0.54	0.016
Y25	YSG	25	0.01	23	4.6	0.25	0.024
W50	WR	50	1.00	9	215	0.55	22
B80	BSG	80	0.01	55	28	0.97	0.79
S20	RSG	20	1.00	16	2.5	0.28	0.015
S40	BSG	40	1.00	15	74	0.54	1.3

Woosley and Heger (2007). These progenitors have been used in black hole formation simulations (e.g., O'Connor 2015; Pan et al. 2018) and in a code-comparison study of 1D core-collapse supernova codes (O'Connor et al., 2018), providing calibration values.

After O'Connor and Ott (2011) found a correlation between the core compactness parameter and BH formation susceptibility, this parameter has often been used for predicting explodability. In the simulations by Ugliano et al. (2012), for a compactness of $\xi_{2.5} < 0.15$ there were only explosions, for $\xi_{2.5} > 0.35$ only BH formation, and a mix of outcomes at values of $\xi_{2.5}$ in between. This was later recalculated by Ertl et al. (2016) with higher resolution and shown to align with the predictions until that point in time. Since there is still ongoing work regarding the predictive value of core compactness with respect to BH formation, we discuss the effects of compactness in our work in Chapter 3.

2.2.1 Generating the progenitors in MESA

In total, we have nine different progenitors, seven that were generated using MESA and two (s20 and s40) that were obtained from Woosley and Heger (2007). We regenerated the seven MESA progenitors from the publicly available input parameter files mentioned above and evolved them from zero-age main sequence (ZAMS) until the onset of core collapse, defined as the moment at which the maximum infall velocity reaches $10^8\,\mathrm{cm\,s^{-1}}$. At the end of each simulation, MESA creates a file called "final_profile.data," which contains all the hydrostatic information about the star at the end of the simulation. Using Python scripts that read this file, I generated the necessary "*.short" input files for GR1D, the function of which is explained in Section 2.3. GR1D uses this "*.short" file to regenerate the inner domain of the star before hydrodynamically evolving it.

The s20 and s40 progenitors were originally created in KEPLER, a code with similar functions to MESA for our purposes. The profiles were downloaded from the author's website[2]. We used a Python script that reads the KEPLER outputs to generate the same "*.short" input files for GR1D as those from MESA.

2.3 Inner core evolution using GR1D

The evolution of the inner stellar core from collapse until black hole formation is modeled with the spherically-symmetric neutrino radiation-hydrodynamics code GR1D[3] version 1 (O'Connor and Ott, 2010). The code solves the equations of general-relativistic hydrodynamics in spherical coordinates using the radial gauge, polar slicing metric (Romero et al., 1996). The finite-volume hydrodynamics solver employs a piecewise-parabolic reconstruction, and performs a temporal update using a second-order Runge-Kutta scheme.

During collapse, neutrino effects are modeled via a parameterization of the

[2] https://2sn.org/sollo03/

[3] Available at stellarcollapse.org

electron fraction with density (Liebendörfer, 2005). After bounce, neutrino cooling in this version of GR1D is modeled with a gray leakage scheme for $\nu_{\rm e}$, $\bar{\nu}_{\rm e}$, and a composite heavy lepton neutrino $\nu_{\rm x}$. The opacity has contributions from charged-current absorption on nucleons and neutral-current scattering on nucleons and nuclei. Emission accounts for charged-current reactions and thermal emission from neutrino pair annihilation and plasmon decay. The local effective emission rate is an interpolation between the diffusive and free emission rates (e.g., Rosswog and Liebendörfer 2003). Neutrino heating due to charge current absorption is computed from the enclosed local luminosity obtained from the leakage scheme. The local outgoing luminosity is then corrected for the neutrino energy lost to heating.

2.3.1 GR1D Simulations

We consider three finite-temperature equations-of-state (EOSs) in our calculations: SFHo (Steiner et al., 2013) as our default (soft) case; DD2 (Hempel et al., 2012) as a stiff variant; and LS220 (Lattimer and Swesty, 1991) as a reference case as it is often used in supernova literature. The maximum mass of cold ($T = 0\,\mathrm{K}$) NSs for DD2 EOS is $2.42\,\mathrm{M}_\odot$ and $2.06\,\mathrm{M}_\odot$ for both the SFHo and LS220 EOSs. These EOSs are commonly used in the core-collapse supernova and NS merger literature (e.g., Pan et al. 2018; Vincent et al. 2019), thus providing a connection to previous work (while DD2 and SFHo are consistent with experimental and observational constraints, as well as with unitary gas bounds on the symmetry energy and its density derivative, LS220 is not; see Tews et al. 2017).

The three tabulated EOSs used in the GR1D simulations were downloaded from a public repository[4]. The code uses a file called "parameters," within which is all the necessary information for the simulation: grid set-up; hydrody-

[4]https://stellarcollapse.org/equationofstate

namics; EOS used; neutrino evolution; atmosphere; and rotation parameters. We created three different simulations per fiducial progenitor — one for each different EOS. For the rest of the progenitors, we created one simulation using the SFHo EOS so that we can explore the effects of different progenitors, with the exception of the $80\,M_\odot$ BSG with which we also tested the DD2 EOS, as that model failed in F18 and a stiffer EOS may have changed the outcome.

In most models, the computational domain is discretized with a uniform grid of 200 cells from the origin out to 20 km, and logarithmic spacing for larger radii, for a total grid size of 1000 cells. In RSG models we double the resolution in the uniform section of the grid ($r < 20\,\mathrm{km}$) as these models take longer to reach BH formation and reach more compact shock radii. The maximum radius in the domain is set by a density close to the lowest value in the tabulated EOS ($2 - 3 \times 10^3\,\mathrm{g\,cm^{-3}}$), corresponding typically to a few times $10^9\,\mathrm{cm}$, much smaller than the radius of the star at core-collapse. The dynamical time at the outer boundary is typically $\sim 10\,\mathrm{s}$, which is much longer than the time to form a BH in most models, justifying our approximation of neglecting the evolution of the outer stellar layers when evolving the core with `GR1D`.

Simulations are deemed to have formed a BH when the density increases rapidly with time to values $\sim 1-3\times10^{15}\,\mathrm{g\,cm^{-3}}$, at which point the simulation stops. In only one case (model R15 with a DD2 EOS) we fail to reach BH formation within $\sim 4.36\,\mathrm{s}$ of evolution, after which the simulation stops when the Courant-Friedrichs-Lewy condition reaches a maximum, although based on the central value of the lapse function (0.44), the model is close to BH formation.

While a newer version of `GR1D` is available, which treats neutrinos with a multigroup moment (M1) scheme (O'Connor, 2015) and therefore provides a more accurate measure of mass-energy lost, the convergence of the transport algorithm near black hole formation in this version is more fragile than that of

the leakage scheme. For a thorough discussion on our reasons for using `GR1D` Version 1 over Version 2, see Appendix C.

2.4 Response of the star to neutrino mass loss

The hydrodynamic response of the outer layers of the star to neutrino mass loss in the core is modeled with the Newtonian hydrodynamics code `FLASH` Version 3 (Fryxell et al., 2000; Dubey et al., 2009), with the modifications described in Fernández (2012) and F18. The code solves the Euler equations;

$$\frac{\partial \rho}{\partial t} + \frac{1}{r^2}\frac{\partial}{\partial r}\left(r^2 \rho v_r\right) = 0 \ , \tag{2.3}$$

$$\frac{D v_r}{D t} + \frac{1}{\rho}\frac{\partial p}{\partial r} - \mathbf{g}_{\rm F}(r,t) = 0 \ , \tag{2.4}$$

$$\frac{D e_{\rm int}}{D t} - \frac{p}{\rho^2}\frac{D \rho}{D t} = 0 \ , \tag{2.5}$$

where ρ, v_r, $e_{\rm int}$, p, and $\mathbf{g}_{\rm F}(r,t)$ are the fluid density, radial velocity, specific internal energy, pressure, and gravitational acceleration at radius r, respectively, and

$$\frac{D}{D t} \equiv \frac{\partial}{\partial t} + v_r \frac{\partial}{\partial r} \ . \tag{2.6}$$

The equations are solved in spherical symmetry with the dimensionally-split Piecewise Parabolic Method (PPM; Colella and Woodward 1984, Fryxell et al. 1989) and the Helmholtz EOS (Timmes and Swesty, 2000).

The computational domain spans a radial interval $[r_{\rm in}, r_{\rm out}]$ that varies for different evolution modes and progenitors, as explained below. It is discretized with a logarithmic grid using a resolution of $2,048$ cells per decade in radius ($\Delta r/r \simeq 0.11\%$) for RSG, YSG, and BSG models, and double that value

($\Delta r/r \simeq 0.06\%$) for WRs. At this resolution, the pressure scale heights at the surfaces of all progenitors are well resolved. We also evolve models with a lower resolution of 512 cells per decade in radius ($\Delta r/r \simeq 0.45\%$) to compare with the results of F18, which used this value as their highest resolution. The boundary conditions are set to outflow at $r = r_{\rm in}$ and $r = r_{\rm out}$. The mass flowing into the inner boundary is kept track of as a scalar baryonic mass $M_{\rm B,flash}$, such that total mass is conserved close to machine precision (F18).

The gravitational acceleration in FLASH $\mathbf{g}_{\rm F}$ is a sum of the contribution from the (baryonic) mass in the computational domain and the gravitational mass $M_{\rm G,flash}$ inside $r_{\rm in}$ in FLASH,

$$\mathbf{g}_{\rm F}(r,t) = -\frac{G}{r^2}\left[M_{\rm G,flash} + 4\pi\int_{r_{\rm in}}^{r}\rho(x,t)\,x^2 dx\right]\hat{r}\ . \tag{2.7}$$

Initially, the gravitational mass $M_{\rm G,flash}$ is either equal to the baryonic mass enclosed within $r = r_{\rm in}$ in the presupernova progenitor, or otherwise mapped from `GR1D`, depending on the mode of evolution (see below). This gravitational mass is subsequently updated from time t_n to t_{n+1} by adding the change due to the (baryonic) mass flowing through the inner boundary over the time step, and correcting for the instantaneous difference between baryonic and gravitational masses as computed by `GR1D` or from an analytic fit,

$$\begin{aligned} M^{(n+1)}_{\rm G,flash} &= M^{(n)}_{\rm B,flash} + 4\pi\int_{t_n}^{t_{n+1}}\left[r^2\rho\max(-v_r,0)\right]\Big|_{r_{\rm in}} dt \\ &\quad -\delta M_{\rm G}(t_{n+1}) + \delta M_{G,{\rm gr1d}-0}, \end{aligned} \tag{2.8}$$

where

$$\delta M_{\rm G}(t_n) = M_{\rm B,gr1d}(t_n) - M_{\rm G,gr1d}(t_n)\ ; \tag{2.9}$$

is the instantaneous difference between the baryonic and gravitational masses

Table 2.2: Evolution modes for FLASH simulations.

	$\delta M_{\rm G}(t)$		initial condition
	from GR1D	analytic	from GR1D
Mode 1 - Interpolation	yes	no	no
Mode 2 - Analytic	no	yes	no
Mode 3 - Remap	yes	no	yes

enclosed by $r = r_{\rm in}$ in GR1D ($M_{\rm B,gr1d}$ and $M_{\rm G,gr1d}$, respectively), and $\delta M_{\rm G,gr1d-0}$ $\sim 0.01 M_\odot$ is an initial offset between these two masses (see Figure 2.2). $M_{\rm B,gr1d}$ and $M_{\rm G,gr1d}$ are tabulated in GR1D with respect to time and radius, so I wrote a script which checks the values at $r = r_{\rm in}$, subtracts them from each other at each time step, and tabulates them as a new file that records the time and $\delta M_{\rm G}(t_n)$. Since at the onset of significant neutrino emission we have $M_{\rm G,flash} \simeq M_{\rm G,gr1d} \simeq M_{\rm B,gr1d}$, this formulation preserves consistency in the mass evolution within FLASH, which is entirely baryonic, while also accounting for the mass-energy lost to neutrinos via $\delta M_{\rm G}$. When a BH forms at time $t = t_{\rm bh}$, the mass difference $\delta M_{\rm G}(t_{\rm bh})$ becomes a constant in equation (2.8).

The initial condition for FLASH and the evolution of the inner core ($r < r_{\rm in}$) are treated in three different ways, to assess the sensitivity of our results to the details of the inner core history (Table 2.2).

1. *Interpolation*: by default, we initialize FLASH with the pre-collapse profile from MESA, and interpolate $\delta M_{\rm G}(t)$ at $r = r_{\rm in}$ as a function of time from GR1D. This approach provides a more realistic value for the mass-energy loss to neutrinos relative to the models of F18, while starting from the same initial condition. Figure 2.2 shows the evolution of the mass difference $\delta M_{\rm G}(t)$ for the three fiducial progenitors and EOSs used. The curves start from a very small value ($\delta M_{\rm G,gr1d-0}$) and increase almost linearly until BH formation. The inner radial boundary for these models are located at $r_{\rm in} = 2 \times 10^8\,{\rm cm}$ as in F18 (approximately at the outer edge of the iron core).

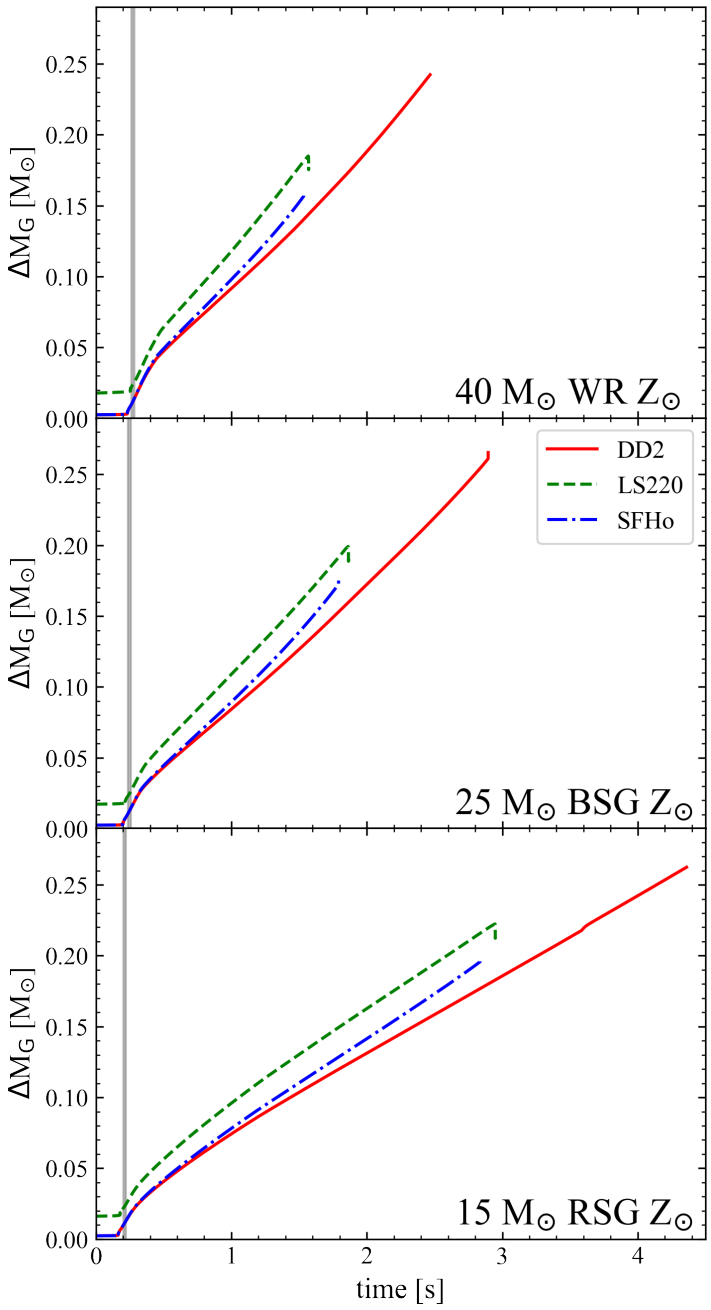

Figure 2.2: Evolution of the difference $\delta M_{\rm G}$ between baryonic and gravitational masses enclosed within $r = 200$ km in `GR1D` as a function of time from the onset of core-collapse. The solid red, green dashed, and blue dashed-dotted lines represent the evolution obtained with the DD2, LS220, and SFHo EOS, respectively. The gray region is defined as the range of times $t_{\rm stall}$ (0.204−0.220s for R15, $0.236 - 0.257$s for B25, and $0.261 - 0.286$s for W40, with the largest values corresponding to the DD2 EOS) at which variables are mapped into `FLASH` when porting the initial condition from `GR1D` (Figure 2.3).

2. *Analytic*: given the overall simplicity of the function $\delta M_{\rm G}(t)$, we evolve a second group of models by initializing the domain in the same way as with the Interpolation mode, but now we parameterize the function $\delta M_{\rm G}(t)$ as a linear ramp that turns on and off at specified times $t_{\rm stall}$ and $t_{\rm bh}$, reaching the same maximum value as the instantaneous function $\delta M_{\rm G}(t)$. The aim is to quantify the degree to which the details of the gravitational mass loss history (as opposed to just the final magnitude and overall timescale) influences the results. The inner boundary for these models is also located at $r_{\rm in} = 2 \times 10^8\,{\rm cm}$.

3. *Remap*: a third group of models where the initial condition for `FLASH` is mapped from `GR1D`, in addition to interpolating the mass difference $\delta M_{\rm G}(t)$ at $r = r_{\rm in}$ as a function of time. Profiles of density, pressure, and composition are mapped at a time $t_{\rm stall}$ when the shock reaches its maximum amplitude, usually $\sim 100 - 200\,{\rm ms}$ after the onset of collapse. At this time, the difference between gravitational and baryonic masses is $\lesssim 0.01 M_\odot$. The inner radius $r_{\rm in}$ of the computational domain in `FLASH` is chosen such that (1) the shock radius in `GR1D` never exceeds it, and (2) the flow at this radius is supersonic. This ensures that there is no hydrodynamic feedback to regions outside this transition. Figure 2.3 shows a snapshot of the velocity in a `GR1D` run of model W40 with the SFHo EOS at the time of mapping into `FLASH`. For this model, $r_{\rm in} = 2 \times 10^7\,{\rm cm}$ and the time of mapping is ~ 270 ms after bounce. This is not our default mode of evolution because global discrepancies between baryonic masses in `FLASH` and `GR1D` at the few percent level are important enough that results become unreliable (Section 3.1). Therefore, this evolution mode is kept for reference only.

The outer radius of the computational domain in `FLASH` is set to be $r_{\rm out} = \{2 \times 10^{16}, 2 \times 10^{15}, 2 \times 10^{14}\}$ cm for RSG/YSG, BSG, and WR progenitors,

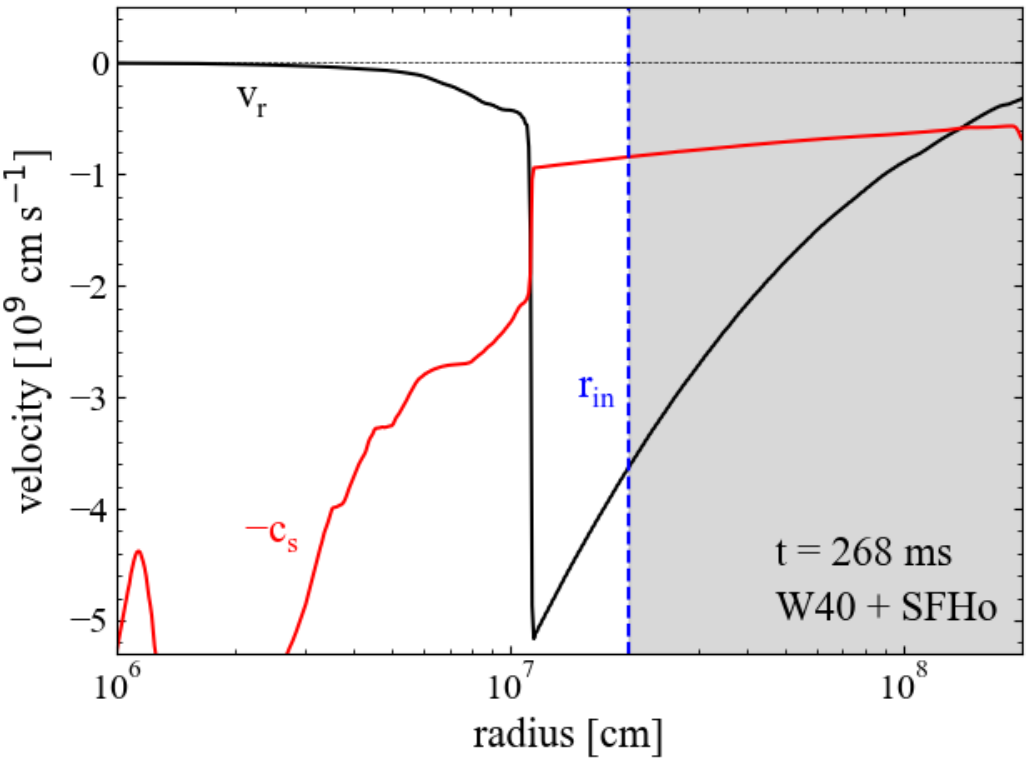

Figure 2.3: Velocity and sound speed as a function of radius in the core-collapse simulation of the W40 progenitor carried out with `GR1D`. The time shown corresponds to that at which, when using *remap* evolution mode (Table 2.2), we map variables into `FLASH` for subsequent evolution ($t_{\rm sim}$ is the time since the onset of core-collapse, and $t_{\rm pb}$ is the time post-bounce (also after bounce)). The vertical blue line indicates the position of the inner radial boundary in `FLASH`.

respectively, corresponding to factors $30 - 1000$ times the stellar surface at core collapse. We fill the domain outside the star with a constant-density ambient medium in hydrostatic equilibrium, with the same composition as the stellar surface. The ambient densities are $\{10^{-18}, 10^{-16}, 5 \times 10^{-13}\}$ g cm^{-3} for RSG/YSG, BSG, and WR progenitors, respectively. These densities are low enough that the ambient mass swept up by the shock is much smaller ($\ll 1\%$) than the ejecta mass itself, with negligible slowdown. While the mass in the ambient for the RSG/YSG models could in principle reach $\sim 0.1 M_\odot$ at the maximum simulation radii, we normally stop our simulations much earlier given that the lowest temperature limit of the Helmholtz EOS is reached. A floor of temperature at 10^4 K is adopted in all simulations, consistent with the low-temperature limit of the Helmholtz EOS. The density floor is set 100 times lower than the ambient for RSGs, YSGs, and BSGs, and a factor of 5 lower than the ambient for WRs, to make sure that when a shock is ejected from the surface of a star, the mass in the ambient is negligible.

2.4.1 From `GR1D` to `FLASH`

After completion, the `GR1D` simulations produce "*.xg" files, which include the entire history of the simulation for each hydrodynamic quantity (e.g. "rho.xg" includes the information about the density for all radial zones at a specific subset of time steps). To include the effects of neutrino mass loss, the baryonic and gravitational masses from `GR1D`, $M_{\rm B,gr1d}$ and $M_{\rm G,gr1d}$, respectively, are extracted from "mass_bary.xg" and "mass_grav.xg" at $r = r_{\rm in}$ and tabulated as a function of time, $t_{\rm sim,gr1d}$, in a file called "GR1D_masses.txt" for use in the `FLASH` simulations (see Figure 2.2). This functionality (see Section 2.4) is the default mode used when evolving the neutrino mass-loss induced shock.

This mass difference is interpolated in `FLASH` with respect to the time of the simulation $t_{\rm sim,flash}$, since the simulation times differ between `GR1D` and `FLASH`. Due to the high time resolution of the tabulated values in "GR1D_masses.txt,"

as well as the overall simplicity of $\delta M_{\rm G}(t)$, we use a simple linear interpolating function to incorporate the neutrino mass loss in FLASH. The interpolator first finds two consecutive $t_{\rm sim,gr1d}$ values within which $\rm t = t_{sim,flash}$, so $t_1 < t_{\rm sim,flash} < t_2$, where $t_{1,2}$ are the indices of the first (lower) and second (higher) of the two consecutive $t_{\rm sim,gr1d}$ values respectively. Then, for each of $\rm M_{bary}$ and $\rm M_{grav}$, the interpolator finds an interpolated mass at $t_{\rm sim,flash}$, such that

$$M_{\rm interp} = \left(\frac{M_2 - M_1}{t_2 - t_1} \right) t_{\rm sim,flash} + M_1 \ , \tag{2.10}$$

where $M_{1,2}$ are defined similarly as for $t_{1,2}$, but for the mass, and $M_{\rm interp}$ is the interpolated mass. This interpolator is used twice at each time step in FLASH, once to calculate $\rm M_{bary}$, and once for $\rm M_{grav}$. These interpolated values for the baryonic and gravitational masses are the ones used in Equation 2.9. $\delta M_{\rm G}$ is then calculated as the difference between the two interpolated masses (including also the initial offset $\delta M_{\rm G,gr1d-0}$). FLASH then subtracts this difference from its own baryonic mass so that the effect is realized in the simulation.

The analytic mode uses the same code in FLASH to incorporate the difference in masses, except that the full GR1D mass-loss history which is recorded in "GR1D_masses.txt" is never used. Instead, three parameters define an analytic ramp function: (i) the time at which the ramp starts, which we define as when the accretion shock stalls $\rm t_{stall}$, the time at which the ramp stops, which we define as the time of black hole formation $\rm t_{bh}$, and the difference in masses at BH formation $\delta M_{\rm G}(t_{\rm bh})$. The resulting analytic $\delta M_{\rm G}(t_n)$ is then incorporated into FLASH in the same way as in Equation 2.8.

To remap the evolution of the inner core of the star into FLASH, I wrote a Python script to read several more "*.xg" files to generate a large table called "GR1D_table.dat," which includes radius, density, velocity, pressure, baryonic mass, and temperature. Any other hydrodynamic quantities FLASH requires are computed using its own EOS solver and the given values from the table. The Python script finds the time at which the shock stalls and at that specific

index of time is when "GR1D_table.dat" is generated.

Since the FLASH simulations for the remap mode start when the GR1D domain is remapped, the initial value of $t_{\rm sim,flash}$ for this mode is different than those of Mode 1 and 2. The remapping happens at the time when the shock stalls, so $t = t_{\rm sim,flash}$ for Mode 1 and 2 and $t = t_{\rm sim,flash} + t_{\rm stall}$ for Mode 3. This is accounted for when calculating $t_{\rm bh}$ in Table 3.1.

When the remapping is completed and the simulation begins, some hydrodynamic variables imported are linearly interpolated to $t_{\rm sim,flash}$, while others use log-log interpolation (such as density and pressure). The rest of the necessary hydrodynamic variables required by the simulation are calculated using the existing interpolated values. The simulation is evolved until $\rm M_{grav}$ reaches the maximum possible mass ($\rm M_{TOV}$), at which point the difference between $\rm M_{grav}$ and $\rm M_{bary}$ is set to a constant value.

We noticed that when we remapped the domain from GR1D into FLASH, there were major differences when compared to Mode 1 and 2 (see Table 3.1). In the $\sim 200\,$ms that passes from core collapse to when the shock front stalls at its maximum radius, and therefore at the time of remapping, there is difference of $\sim 0.1\,\rm M_\odot$ in the enclosed baryonic mass at the outermost mapping radius of $\sim 10^9\,$cm. This is a consequence of the difference in the density profile between FLASH and GR1D. We discuss this more thoroughly in Section 3.1, though in essence this inconsistency physically arises from remapping a GR domain into the domain of a Newtonian code. The mass discrepancy introduced affects the hydrodynamic shock produced in unphysical ways and is large enough to make our remapping results in Mode 3 unreliable.

2.4.2 Tracking the shock

During the analysis, one of our main points for this work was whether or not the hydrodynamic shock generated by the neutrino mass-loss ejected significant amounts of mass and energy. In our simulations, the shock manifests itself as

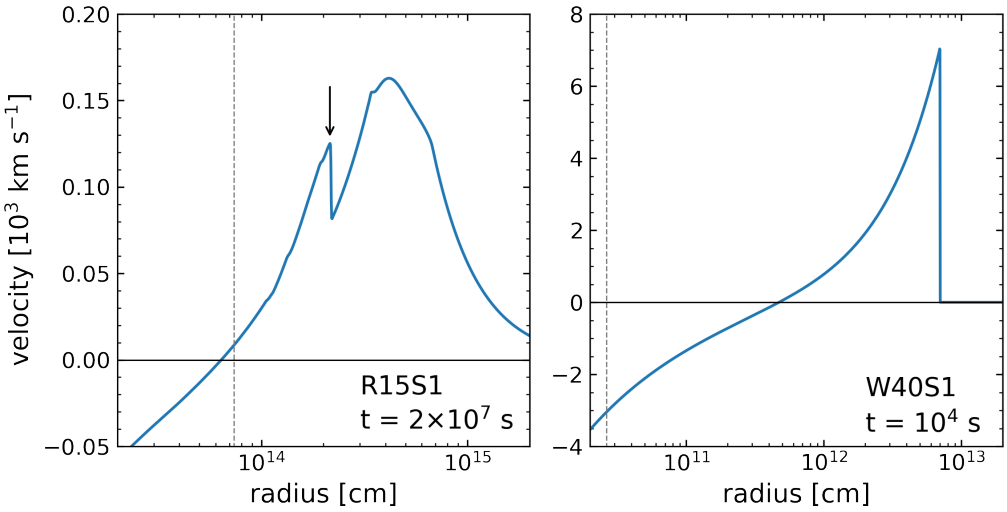

Figure 2.4: Radial velocity as a function of radius for the 15 $M_\odot$ RSG (left) and the 40 $M_\odot$ WR (right) progenitors at the times listed in the plot. The horizontal solid black line depicts the $v_r = 0$ condition we use to label the trailing edge of the shock. The vertical dotted black line is set at the stellar surface R_{cc}. The time in the simulation is printed in the bottom right of both plots. The vertical black arrow in the left plot points to the leading edge of the shock generated by neutrino mass loss.

a clump of material with positive radial velocity, and so the analysis script uses one of two methods to track the shock using its velocity profile. For both methods, the tracking of the shock is calculated at each recorded time step (in reality, the script loops over all "plot" files generated by `FLASH`, which are outputted at specific times). The default method at each time step is as follows:

1. Find the radial index of the maximum velocity $v_{\rm max}$.

2. If the maximum velocity is positive, then continue.

    - If the maximum velocity is negative, then there is no outwardly moving shock to track. In this case, the script skips the shock tracking function.

3. Scan radial indices outwards from $r_{\rm in}$ and record the first index where velocity is positive ($v_{\rm r} > 0$).

- This is recorded as the lower edge (or the trailing edge) of the shock.

4. Scan radial indices outwards from the maximum velocity and record the first index where the positive velocity is less than 75% of the maximum ($\frac{3}{4}v_{\rm r} < v_{\rm max}$).

   - This is recorded as the upper edge (or the leading edge) of the shock.

The only difference between the default method and the alternative method is in how the upper edge of the shock is calculated. In the alternative method, the upper edge is recorded as the index where a sufficiently large negative gradient has been reached. The reason for including this second method is because in some cases, the ambient material near the surface of the star reaches positive velocities that result in a noticeable displacement by the time the shock gets to it. This can be clearly seen for the RSG progenitor simulation in Figure 2.4. The ambient low-density material reaches velocities on the order of ~ 150 m/s by the end of the simulation ($t_{\rm sim} = 2 \times 10^7$ s), while the shock can be seen passing through it. The leading edge of the shock is characterized by the steep velocity drop-off right in front of it. In comparison, the WR progenitor simulation at the end of the simulation maintains its clear leading and trailing edges of the shock. For the WR progenitor, the default method of tracking the shock works without any problems. However, the additive nature of the velocities in the RSG simulation makes tracking the shock difficult and using any arbitrary numerical cut-off for the upper edge of the shock may lead to wrong results. So, in those cases, we employ the alternative method that utilizes the sharp velocity gradient at the leading edge. Once the script finds a sufficiently large negative gradient in the velocity, it records it as the leading edge of the shock. This problem only generally arises after the shock leaves the surface of the star.

2.5 Progenitors Evolved

All of our simulations are listed in Table 3.1. We adopt the SFHo EOS and interpolation of $\delta M_{\rm G}(t)$ from `GR1D` (Table 2.2) as our default choice.

The three fiducial progenitors described in Section 2.2 (R15, B25, W40) are evolved using the three equations of state described in Section 2.3 with progenitor names appended {S,L,D} when using the SFHo, LS220, or DD2 EOS, respectively, and ending in {1,2,3} in accordance to the inner core evolution modes listed in Table 2.2. For example, model R15S1 is the R15 progenitor evolved with the SFHo EOS in `GR1D` interpolating $\delta M_{\rm G}(t)$ into `FLASH`. We also evolve the 3 fiducial progenitors varying the evolution mode of the inner core, using the SFHo EOS. The remaining progenitors are all evolved using the SFHo EOS and interpolation of $\delta M_{\rm G}(t)$.

Each progenitor is evolved at the maximum resolution listed in section 2.4, as well as at a lower resolution (the highest resolution used in F18) to compare results. The maximum evolution time is set either by the shock emerging from the star and reaching nearly constant total energy, or otherwise when the temperature in the shock reaches the floor value (in which case non-conservation of thermal energy ensues thereafter and results become unreliable).

Chapter 3

Results

3.1 Overview of the evolution for different progenitors

The GR1D simulations of the inner core evolution for all progenitors are qualitatively the same. After core-collapse and bounce, the shock stalls and then gradually recedes on a timescale of $\sim 1\,\mathrm{s}$. This behaviour is expected for non-rotating iron core progenitors evolved in spherical symmetry, as mentioned in Section 2.1 (Liebendörfer et al., 2001; Rampp and Janka, 2002; Thompson et al., 2003; Sumiyoshi et al., 2005). With the exception of model R15D1, a black hole forms within less than 3 s after bounce. At the time of BH formation, the difference between baryonic and gravitational masses δM_{G} is set to a constant, as shown in Figure 2.2.

At a radius $\sim 10^9\,\mathrm{cm}$, where the local free-fall time t_{ff} is comparable to the time that the gravitational mass changes due to neutrino cooling, $\sim t_{\mathrm{bh}}$, a sound pulse forms. This sound pulse steepens into a shock and it quickly reaches a speed of about Mach 1 (F18; Coughlin et al. 2018a), after which its speed increases even further. The subsequent evolution of this shock and its effect on the stellar envelope depends on the type of stellar progenitor. Table 3.1

Table 3.1: Table of hydrodynamic models from `GR1D` v. 1.03 and summary of the highest resolution `FLASH` runs, see Section 3.4 for dependence of these results on spatial resolution. Columns from left to right show the model name, time to BH formation from the onset of core-collapse $t_{\rm bh}$, maximum gravitational mass lost to neutrinos $\delta M_{\rm G}(t_{\rm bh})$, maximum kinetic energy of the shock in `FLASH` $E^{\rm sim}_{\rm k,max}$, total mass ejected in `FLASH` $M_{\rm ej}$, total energy of ejecta $E_{\rm ej}$, and hydrogen recombination energy $E_{\rm rec}$ (Equation 3.4) for stars with extended hydrogen envelopes. The special model "W40S1.7" has $r_{\rm in} = 2 \times 10^7\,{\rm cm}$, instead of the default $r_{\rm in} = 2 \times 10^8\,{\rm cm}$ used for *interpolation* mode.

Model	$t_{\rm bh}$ (s)	$\Delta M_{\rm G}$ ($M_\odot$)	$E^{\rm sim}_{\rm k,max}$ ($10^{47}\,{\rm erg}$)	$M_{\rm ej}$ ($M_\odot$)	$E_{\rm ej}$ ($10^{47}\,{\rm erg}$)	$E_{\rm rec}$ ($10^{47}\,{\rm erg}$)
R15S1	2.836	0.196	2.15	2.19	-0.119	0.398
R15S2			2.06	2.16	-0.154	0.388
R15S3			0.57	0.99	-0.268	0.179
R15L1	2.947	0.222	2.42	2.42	-0.103	0.440
R15D1	>4.359	>0.262	3.59	3.37	0.489	0.612
S20S1	2.188	0.173	0.69	0.70	-0.320	0.128
				$M_{\rm ej}$ ($10^{-2}\,{\rm M}_\odot$)		
B25S1	1.791	0.173	2.27	2.80	0.399	
B25S2			2.27	2.82	0.404	
B25S3			0.14	0.45	0.012	
B25L1	1.864	0.198	2.55	3.18	0.593	
B25D1	2.895	0.261	5.40	5.45	1.76	
Y22S1	0.931	0.139	0.55	5.39	-0.013	0.010
Y25S1	2.542	0.175	3.18	15.5	-0.082	0.028
				$M_{\rm ej}$ ($10^{-4}\,{\rm M}_\odot$)		
W40S1	1.535	0.157	1.40	1.44	0.067	
W40S2			1.36	1.36	0.063	
W40S3			0.06	0.01	<0.001	
W40L1	1.570	0.184	1.52	1.63	0.077	
W40D1	2.466	0.242	3.92	6.30	0.326	
W40S1.7	1.535	0.157	1.68	1.91	0.090	
W50S1	0.895	0.126	0.53	0.54	0.019	
B80S1	0.624	0.074	0.09	0.76	-0.001	
B80D1	0.706	0.115	0.21	2.13	-0.002	
S40S1	0.943	0.128	0.13	1.07	<0.001	

summarizes the results of our hydrodynamic simulations.

For all models in which we remapped the domain of GR1D into FLASH, there are discrepancies that are $\leq 10\%$ in the fluid quantities from GR1D at $t = t_{stall}$ (slightly lower density, lower internal energy, differing infall velocity) at the mapping radius r_{in}. This results in the remapped models collapsing faster relative to the models that only make use of $\Delta M_G(t)$ to modify gravity (evolution modes 1 and 2), which yield reduced kinetic energy of the shock and lower amount of mass ejected (models R15S3 and B25S3) or no mass ejected at all (model W40S3). Separately evolving FLASH up to the time of remapping in GR1D ($\sim 270\,\mathrm{ms}$) makes a negligible difference in the enclosed baryonic mass at the transition radius before remapping.

Resolving this discrepancy requires a self-consistent treatment of the entire star using general-relativity, which is beyond the scope of our study. We therefore adopt the interpolation of $\delta M_{\mathrm{G}}(t)$ from GR1D as our default evolution mode in the rest of this paper.

Figure 3.1 shows the evolution of the energy components in the shock generated by neutrino mass loss as it travels outward through the envelope for our three fiducial progenitors. The methods for determining the shock boundaries and thus the key properties of the shock within are described in Section 2.4.2. The mass in this shock changes with time; it sweeps up mass at its front as it travels outwards and loses mass at its back to fallback accretion. In all cases, the kinetic energy in the shock is initially a small fraction of the gravitational and internal energies. As the shock propagates radially outwards, the kinetic energy eventually becomes comparable and/or exceeds the thermal and gravitational energies as it emerges from the stellar surface. The final net energy of the outgoing shock is comparable to its initial kinetic energy.

The propagation of weak shocks in gravitationally bound stellar envelopes does not conserve energy (Coughlin et al., 2018b). Depending on the radial dependence of the stellar density profile and on the initial strength of the

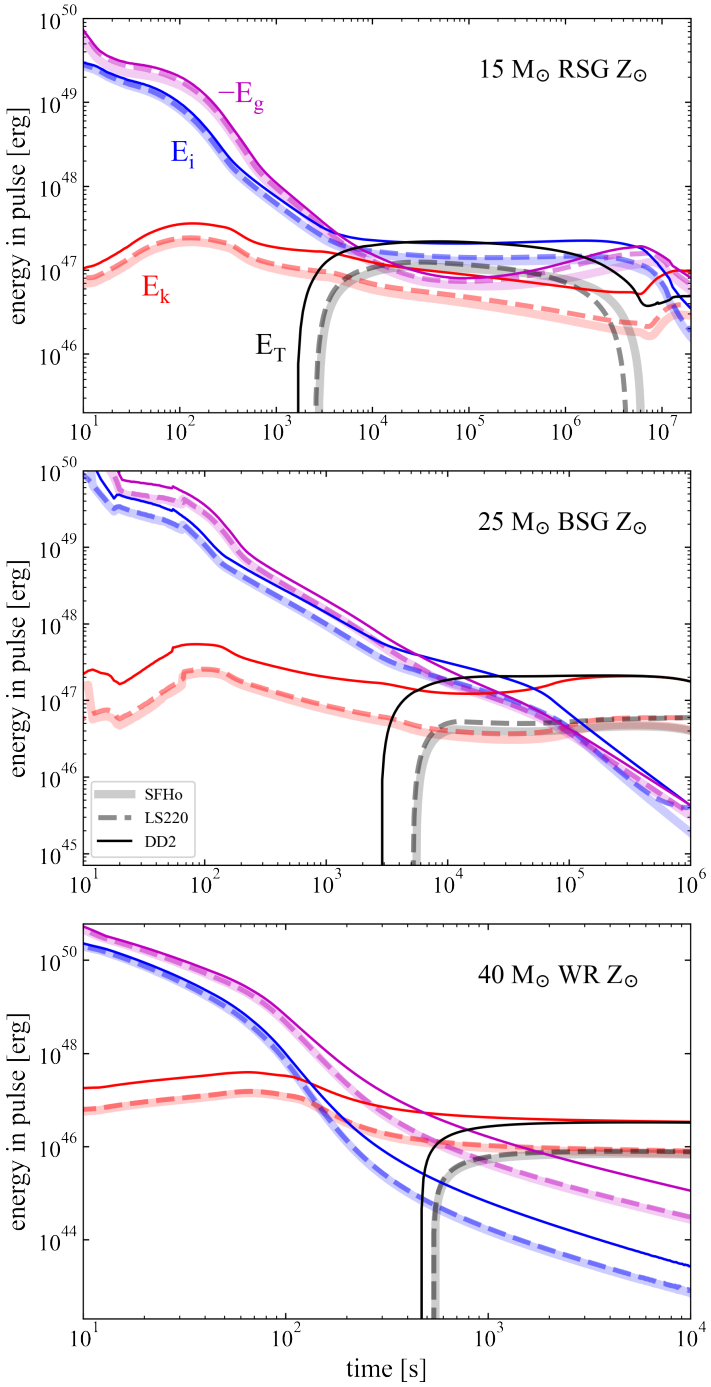

Figure 3.1: Evolution of the energy components in the shock generated by neutrino mass-energy loss for our three fiducial progenitors: R15 (top), B25 (middle), and W40 (bottom). Each panel shows the kinetic (red), internal (blue), gravitational (purple), and total energy (black) for models that interpolate $\delta M_{\rm G}$ from `GR1D` and vary the EOS: DD2 (thin solid), SFHo (thick semitransparent), and LS220 (dashed). Only positive total energies are shown.

shock, the shock can accelerate or decelerate, producing behavior that ranges from a strong shock as it reaches the stellar surface to dying off as a rarefaction wave that ejects a negligible amount of mass (Coughlin et al., 2019; Ro et al., 2019).

The energy of the shock can be understood, to order of magnitude, from the impulse $\delta v_{\rm shell}$ imparted by the change in gravity over a free-fall time $t_{\rm ff}$,

$$\delta v_{\rm shell}(r) = \frac{G\,\delta M_{\rm G}}{r^2}\,t_{\rm ff} \tag{3.1}$$

(Coughlin et al. 2018a, F18). The kinetic energy of a stellar shell of thickness $H_{\rm p}$ is

$$\delta E_{\rm shell} \simeq \frac{1}{2}\,M_{\rm shell}\,\delta v_{\rm shell}^2, \tag{3.2}$$

with $M_{\rm shell} \simeq 4\pi r^2 \rho H_{\rm p}$, where ρ is the density profile of the shock and $H_{\rm p}$ is the pressure scale height. In terms of stellar quantities, we can write the maximum kinetic energy that a shell can have as (F18)

$$\begin{aligned} E_{\rm k,\,max} \simeq \quad & 2.5\times10^{47}\left(\frac{\alpha}{0.4}\right)\left(\frac{H_{\rm p}/r}{0.4}\right)\left(\frac{\delta M_{\rm G}}{0.15 M_\odot}\right)^2 \\ & \times\left(\frac{2\times10^9\,{\rm cm}}{r}\right)\,{\rm erg}. \end{aligned} \tag{3.3}$$

where $\alpha \equiv d\ln M(r)/d\ln r$. We evaluated Equation 3.2 at the point of shock formation, where the kinetic energy generated is maximum. The maximum kinetic energies obtained in the simulations (Figure 3.1, also shown in Table 3.1 as $E_{\rm k,max}^{\rm sim}$) roughly agree with Equation 3.3 given the characteristic gravitational mass changes $\delta M_{\rm G}(t_{\rm bh})$ shown in Table 3.1.

The mass ejected is set, to order of magnitude, by the exterior mass coordinate in the star at which the gravitational binding energy is comparable to the shock energy. RSGs, with weakly bound hydrogen envelopes, can eject

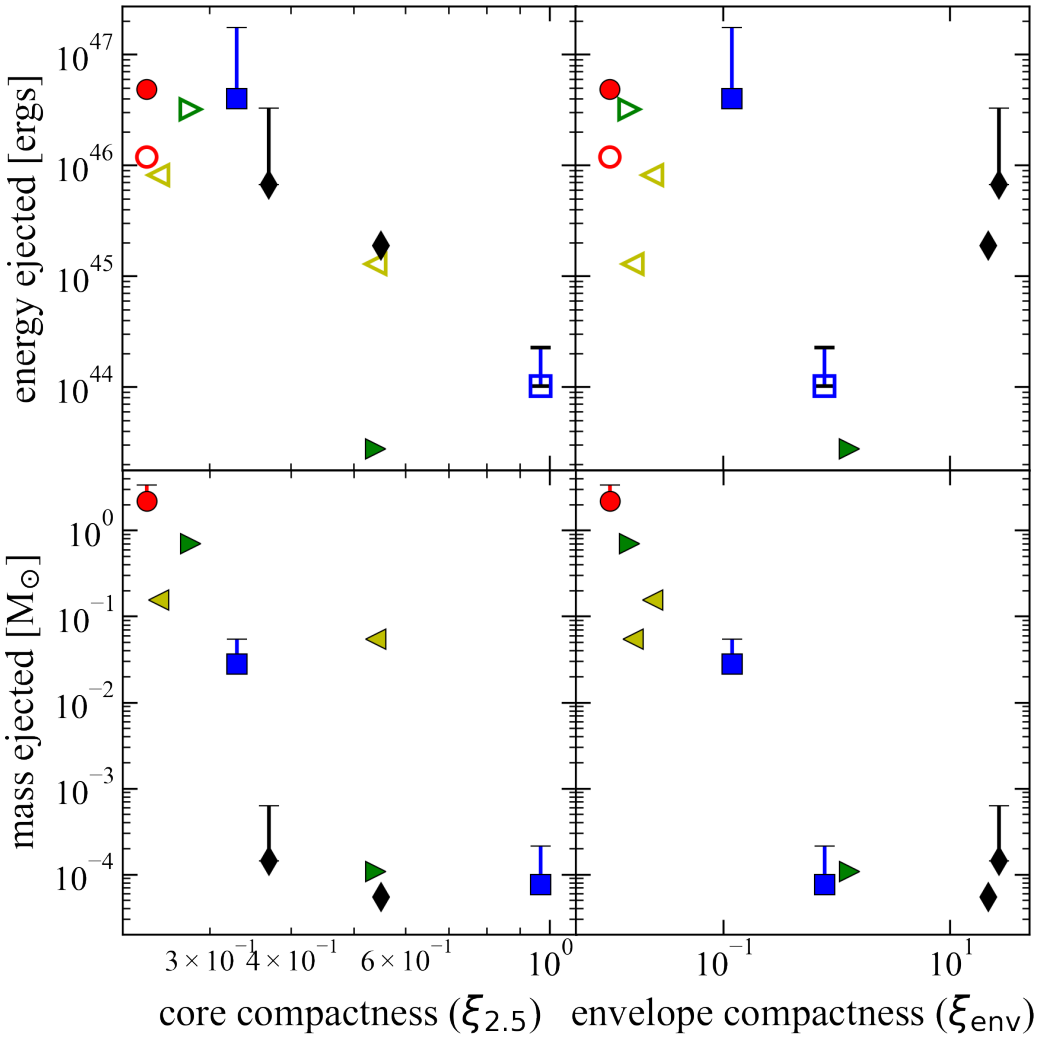

Figure 3.2: Ejecta energy (top) and mass (bottom) as a function of core compactness $\xi_{2.5}$ (left) and envelope compactness $\xi_{\rm env}$ (right) for all models that interpolate $\delta M_{\rm G}(t)$ from `GR1D` using the SFHo EOS. The error bars indicate the difference introduced by evolving the inner core with the DD2 and LS220 EOSs (for our three fiducial progenitors) and only DD2 for the B80 progenitor. Colored markers correspond to their respective progenitors: red circles for RSGs, blue squares for BSGs, black diamonds for WRs, yellow left triangles for YSGs, green right triangles for S20 and S40 models. Open and full symbols in the top row denote bound and unbound ejecta, respectively, with the exception of the R15 models, for which we have plotted both R15S1 (open circle, bound) and R15D1 (full circle, unbound).

several solar masses of slowly-moving material (Lovegrove and Woosley, 2013), whereas BSGs and WR stars eject much smaller masses at higher speeds (F18).

Figure 3.2 shows the mass ejected and ejecta energies as a function of core compactness, Equation 2.1, and envelope compactness, Equation 2.2, for all of our simulations that interpolate $\delta M_{\rm G}(t)$ from `GR1D` and use the SFHo EOS. Between all four correlations, the strongest (by eye) is an inverse correlation between ejected mass and envelope compactness (Figure 3.2, bottom right). This means that given shock energies of characteristic magnitude $\sim 10^{47}$ erg, the mass ejected is inversely proportional to the surface gravity of the star.

In Figure 3.3 we show the maximum gravitational mass lost to neutrino emission as a function of core compactness. The overall trend is that there is a monotonic decrease in $\delta M_{\rm G}(t_{\rm bh})$ with increasing compactness, which is representative of the inverse dependence of the ejecta energy with core compactness (Figure 3.2, top left). Higher compactness is associated with a shorter time to BH formation (O'Connor and Ott, 2011; da Silva Schneider et al., 2020), which would result in less mass-energy lost to neutrinos.

While the ejecta energy is weakly correlated with envelope compactness (Figure 3.2, top right), in Figure 3.4 we show a strong correlation (by eye) between the energy per unit mass (and hence velocity) of the ejecta and the envelope compactness. Stars that can unbind matter from their surfaces do so at speeds comparable to the escape velocity at that location.

To illustrate these trends, we compare several different models to each other. Firstly, we can compare models R15S1 and Y22S1, which have similar envelope compactness (0.010 and 0.016 respectively), but where the YSG has more than double the core compactness of the RSG (0.54 versus 0.24, respectively). Model R15S1 ejects about $2.2\,{\rm M}_\odot$, almost 40 times more than the YSG ejecta ($5.39 \times 10^{-2}\,{\rm M}_\odot$), which follows from the larger value of $\delta M_{\rm G}(t_{\rm bh})$ for the RSG. In both cases the ejecta is bound without accounting for hydrogen recombination energy. With the recombination energy included, the ejecta would be

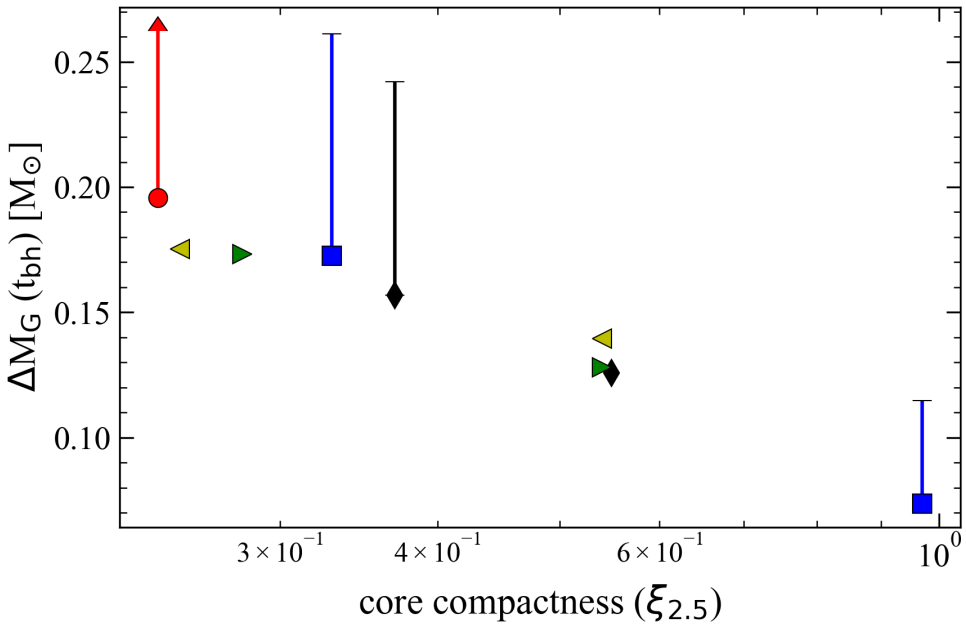

Figure 3.3: Maximum gravitational mass lost to neutrino emission $\delta M_{\rm G}(t_{\rm bh})$ as a function of core compactness $\xi_{2.5}$. Symbols and error bars have the same meaning as in Figure 3.2. An upper limit is used for $\delta M_{\rm G}(t_{\rm bh})$ from model R15D1 since it did not collapse to a BH in `GR1D` within 4.2 s of evolution.

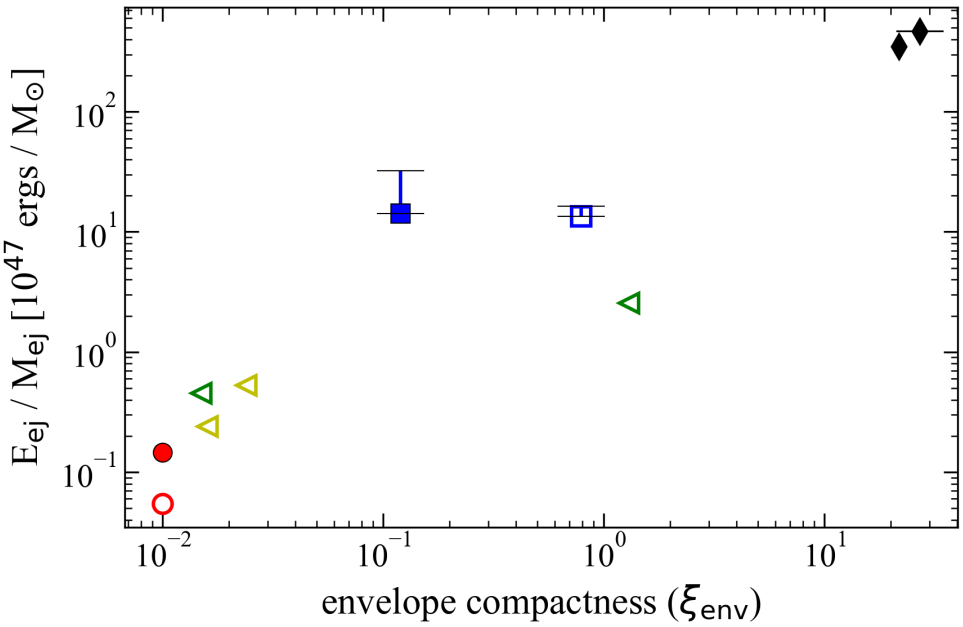

Figure 3.4: Ejecta energy per unit mass as a function of envelope compactness $\xi_{\rm env}$. Symbols and error bars have the same meaning as in Figure 3.2.

unbound. Models R15S1 and Y25S1 have similar core compactness (0.24 and 0.25, respectively), but the YSG's envelope compactness is more than double that of the RSG (0.010 and 0.024, respectively). The Y25 model ejects about $0.16\,M_\odot$, which is approximately 14 times less than the $\sim 2.2\,M_\odot$ from the RSG. In both comparisons, the ejecta is bound before including hydrogen recombination energy, with the energy per unit mass (before hydrogen recombination) being larger in the YSG. And in both comparisons, the YSGs have a higher energy per unit mass compared to the RSG, despite the fact that the RSG ejects more mass overall.

Model B80S1 has a higher core (0.97) and envelope compactness (0.79) than model B25S1 (0.33 and 0.12 respectively). While the B25S1 model ejects $2.8 \times 10^{-2}\,M_\odot$ with 4×10^{46} erg by the end of the simulation, model B80S1 generates a shell with a mass of about $8 \times 10^{-5}\,M_\odot$ that is bound ($E_{ej} \sim -10^{44}$ erg) by the time it approaches the stellar surfaces. That is when the B80 simulation reaches the EOS temperature floor and the internal energy begins rising, leaving subsequent evolution unreliable . This $80\,M_\odot$ progenitor also fails when using parameterized neutrino mass loss in F18. So, while there may be a negative trend that exists between the mass ejected and the core compactness (Figure 3.2, bottom left), there is a limit after which the progenitor will collapse completely without ejecting any mass.

Model W50S1 has a higher core compactness than model W40S1 (0.55 and 0.37 respectively), but a lower envelope compactness (22 and 27, respectively). Model W50S1 ejects less mass and with lower energy ($5.4 \times 10^{-5}\,M_\odot$ with 1.9×10^{45} erg) than W40S1 ($1.4 \times 10^{-4}\,M_\odot$ and 6.7×10^{45} erg). While the energy per unit mass is comparable, it is higher in the W40S1 progenitor which has a lower core and higher envelope compactness.

3.2 EOS Dependence

Table 3.1 shows that for the same stellar model and at fixed resolution, using the stiffer DD2 EOS to evolve the inner core results in more mass ejected and with higher specific energy, by a factor of several, than with the softer SFHo or the LS220 EOS. Equation 3.3 shows that the maximum kinetic energy of the shock is proportional to the square of the gravitational mass lost to neutrinos $\delta M_{\rm G}$. All models evolved with the DD2 EOS achieve higher values of $\delta M_{\rm G}$ than their equivalent models evolved with the SFHo EOS by a factor of up to two. The SFHo and LS220 simulations are usually very similar to each other and often overlap.

The origin of this trend with EOS stiffness is shown in Figure 2.2: the stiffer DD2 EOS yields a longer time to BH formation and therefore results in more gravitational mass lost to neutrino emission than the SFHo EOS. There are some differences in the growth rate of $\delta M_{\rm G}$, associated with the differing neutrino luminosities, which in turn are most sensitive to the effective nucleon masses in the EOS (Schneider et al., 2019). However, these luminosity differences are not the dominant effect compared to the time interval during which the PNS emits neutrinos, which is set primarily by the accretion rate and the maximum mass of a cold non-rotating neutron star ($M_{\rm tov}$) that the EOS can support. The same trend of increasing ejecta mass and energy with increasing $M_{\rm tov}$ was found by Lovegrove and Woosley (2013) using a parameterized evolution of the inner core.

Figure 3.2 shows the spread in ejected masses due to the EOS (represented as error bars) for our three fiducial progenitors. Aside from the magnitude of the gravitational mass lost and a minor change in the location of the shock formation (radius at which $t_{\rm bh} \simeq t_{\rm ff}$), the evolution of the shock as it propagates into the envelope is qualitatively the same for all EOSs, as shown in Figure 3.1.

A key difference introduced by the EOS is that when using SFHo or LS220,

none of the RSG progenitors eject unbound mass (Table 3.1). The equation of state used in `FLASH` assumes fully ionized nuclei, but it is known that hydrogen recombination can dominate the energetics during the expansion of the shock in failed supernovae of RSGs (Lovegrove and Woosley, 2013). To estimate the importance of this missing effect, we compute the recombination energy $E_{\rm rec}$ that can potentially be added to the shock if all the hydrogen contained in the ejecta recombines,

$$E_{\rm rec} = \frac{M_{\rm H}}{m_{\rm p}}\chi_{\rm H} \tag{3.4}$$

$$M_{\rm H} = \int_0^{M_{\rm ej}} X(M)dM, \tag{3.5}$$

with X the mass fraction of hydrogen in the ejecta, $m_{\rm p}$ the proton mass, and $\chi_{\rm H} = 13.6\,{\rm eV}$. The resulting recombination energies for RSGs and YSGs are shown in Table 3.1. With the exception of models S20S1 and R15S3, all RSG progenitors eject unbound material after including this contribution. For YSGs, model Y22S1 can marginally unbind its ejecta when including hydrogen recombination, while model Y25S1 cannot.

We find that our models using the DD2 EOS yield ejecta properties that agree with those of F18, which were obtained using a parameterized evolution of the inner core and therefore of $\delta M_{\rm G}(t)$. In contrast, results obtained with the softer SFHo EOS have energies lower by a factor of several compared to F18. A side-by-side comparison of the same fiducial progenitors is shown in Table 3.2. The relation between the two sets of results follows from the fact that F18 assumed $M_{\rm tov} = 2.5\,{\rm M}_\odot$ as an input in the parametric neutrino scheme. The maximum NS mass at an entropy of $4k_{\rm B}$ per baryon correlates well with $t_{\rm bh}$ when comparing among different EOSs (Hempel et al., 2012). The choice of F18 is much closer to the finite-entropy $M_{\rm tov}$ for the DD2 EOS ($2.57M_\odot$ at $4k_{\rm B}$ per baryon; M. Hempel, private communication) than for the SFHo EOS

Table 3.2: Comparison of the ejecta masses and energies obtained in F18 (high-resolution "e_HR" models, using parametric inner core evolution from Lovegrove and Woosley 2013) and in this work (interpolating $\delta M_{\rm G}(t)$ from `GR1D` using either the SFHo [S1] or DD2 [D1] EOS), for our three fiducial progenitors.

Progenitor	$M_{\rm ej}(M_\odot)$		$E_{\rm ej}(10^{47}\,{\rm erg})$	
	[S1,D1]	F18	[S1,D1]	F18
R15	[2.2, 3.4]	4.2	[-0.1, 0.5]	1.9
B25	[0.03, 0.05]	0.05	[0.5, 1.8]	1.6
W40	$[1, 6]\times10^{-4}$	5×10^{-4}	[0.06,0.31]	0.25

($2.3M_\odot$ at $4k_{\rm B}$ per baryon, Steiner et al. 2013).

3.3 Simplified inner core evolution: analytic ramp

Given the overall simplicity of the $\delta M_{\rm G}(t)$ function, as seen in Figure 2.2, we ran another set of simulations whose purpose was to assess the sensitivity of mass ejection to the detailed history of neutrino emission by the PNS before BH formation. We parameterize $\delta M_{\rm G}(t)$ as a linear ramp in time as explained in Section 2.4.1. Figure 3.5 shows the gravitational mass lost as a function of time, where the black line is the detailed history of neutrino emission and the red line is the linear ramp parameterization. The input parameters are the maximum value of $\delta M_{\rm G}$, the time of BH formation $t_{\rm bh}$, and a starting time that we choose to set at the time when the shock radius reaches its maximum value ($t_{\rm stall}$, same as that used when remapping the domain from `GR1D`). These parameters are generally reported in (or usually straightforward to obtain from) published studies of BH formation in failed SNe.

Figure 3.6 compares the evolution of the energy, mass, and velocities of the shock for models W40S1 and W40S2, with Mode 1 interpolating $\delta M_{\rm G}(t)$ from `GR1D` and Mode 2 using the analytic ramp parameterization. The shock properties are very close to one another in both models, with a few percent

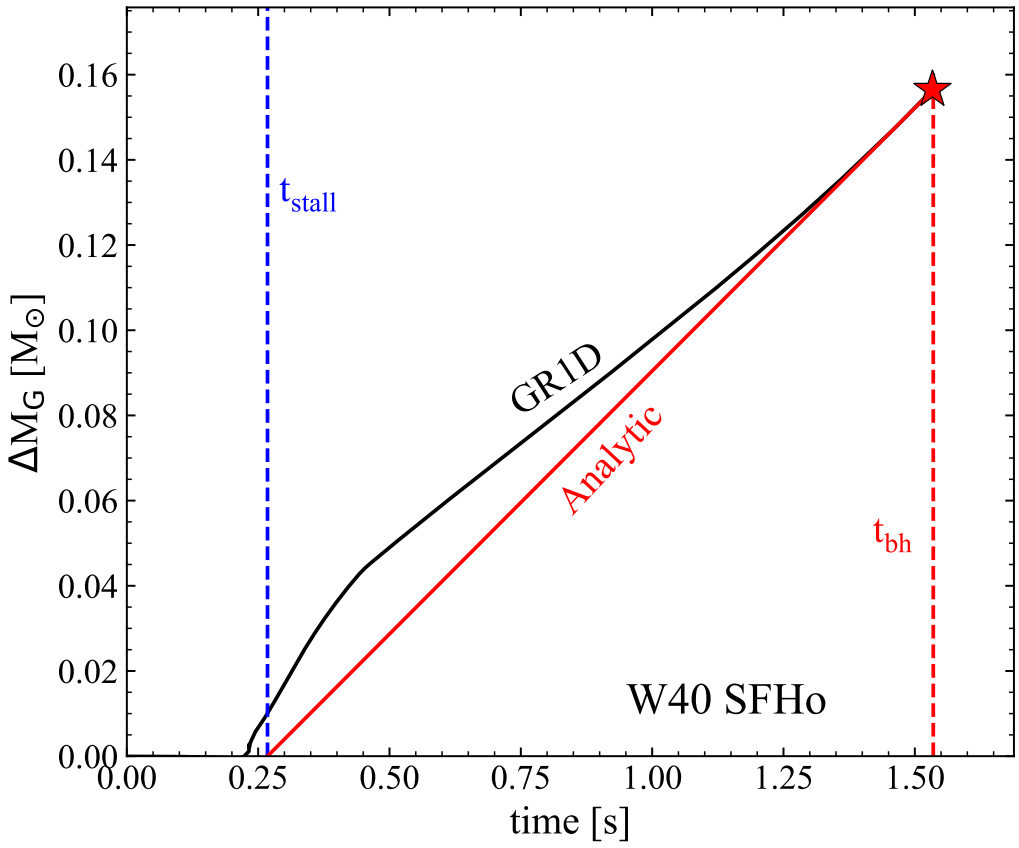

Figure 3.5: Evolution of $\delta M_{\rm G}$ for the W40 progenitor. The result from `GR1D` using the SFHo EOS is shown in black, while our linear ramp parameterization is shown in red, with the star denoting the time of and gravitational mass lost at BH formation. The vertical dashed blue line shows the time $t_{\rm stall}$ at which the shock stalls, which we use to start the ramp function (same time as in Figure 2.3). The vertical dashed red line shows the time of BH formation $\rm t_{bh}$.

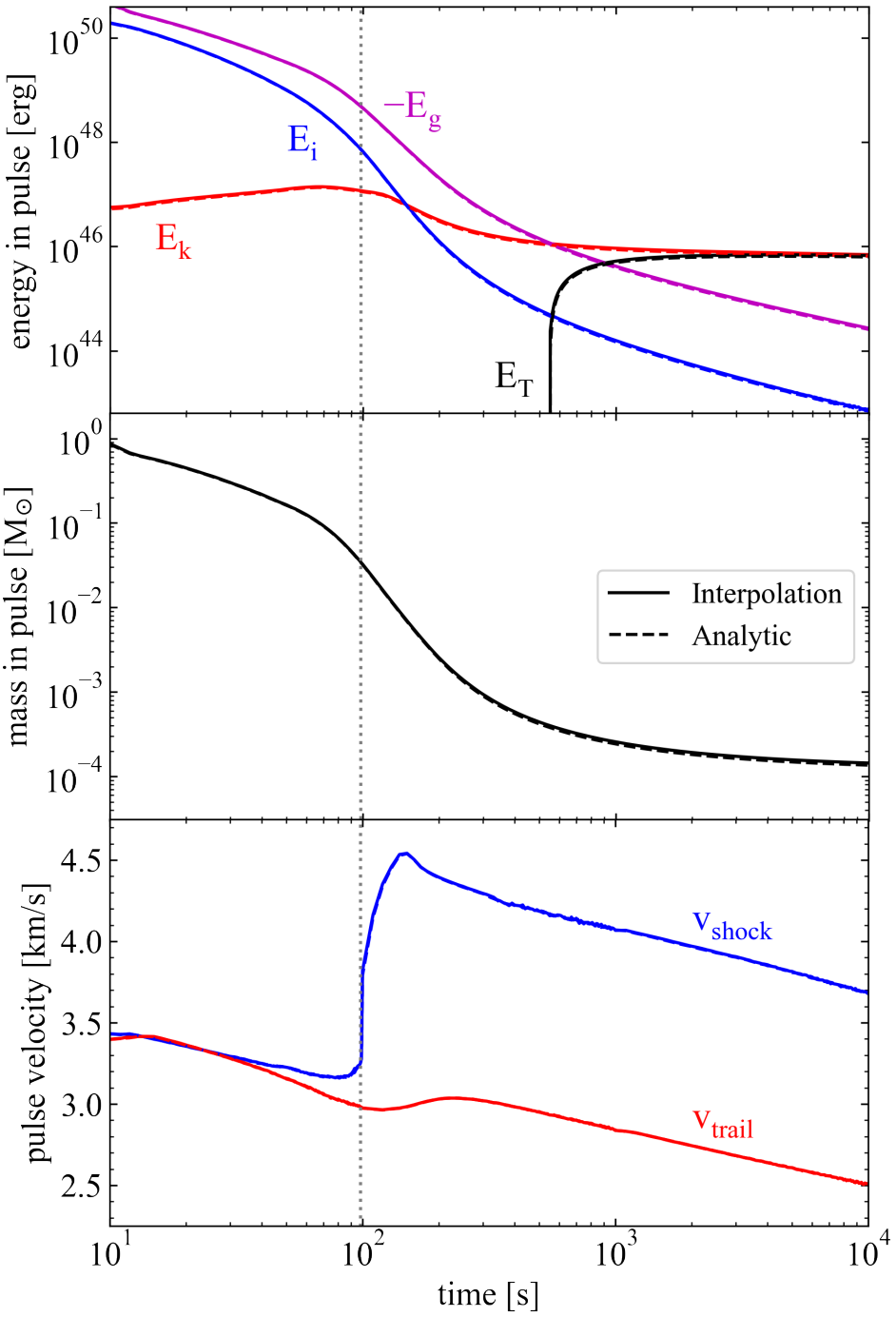

Figure 3.6: Comparison between models W40S1 and W40S2, which interpolate $\delta M_{\rm G}(t)$ from `GR1D` or use an analytic ramp model, as in Figure 3.5, respectively. Top, middle, and bottom panels show the evolution of the energies, mass, and velocity of the shock, as labeled ($v_{\rm shock}$ and $v_{\rm trail}$ are the velocities of the forward and the rear end of the shock, respectively). Thin dotted line represents the time at which the shock emerges from the stellar surface.

difference in ejected mass and ejected energies with increasing resolution. The only exception is the for the RSG that ejected mass with negative energies, so the matter is gravitationally bound, the difference was on the order of 30%.

The low sensitivity to the detailed neutrino history can be understood from the fact that variations in neutrino emission (as inferred from Figure 2.2) occur on timescales much shorter than $t_{\rm bh}$. Mass shells for which the local dynamical time $t_{\rm dyn}$ is comparable to this neutrino variability timescale are accreted into the BH before there is sufficient time to affect the emergence of a sound pulse at a location such that $t_{\rm dyn} \sim t_{\rm bh}$.

3.4 Effect of spatial resolution

Table 3.3 reports the mass ejected and final energy of the shock for our fiducial models at two resolutions: the same resolution used in F18 ("1X": $\Delta r/r = 4.5 \times 10^{-3}$) and at the highest resolution used in our study: for RSG and BSG models, the resolution used was 4 times the grid spacing of F18 ("4X": $\Delta r/r = 11 \times 10^{-4}$), and for WR models, the resolution used was 8 times the grid spacing ("8X": $\Delta r/r = 6 \times 10^{-5}$). For the RSG and BSG models, we find that the difference between our low- and high-resolution results was a maximum of $\sim 1\%$, while the difference for the WR models was much more significant; on the order of $\sim 20\%$.

The main reason for the dominant effect of resolution on the WR models is due to how well the scale height is resolved at the surface of the star. As mentioned in Section 2.4, the scale height is resolved well for all our simulations: at "4X" resolution, we obtain ~ 10 and ~ 17 computational grid cells per scale height for the RSG and BSG models. In comparison, F18 obtained ~ 2 and ~ 4 cells per scale height in their "1X" resolution results. Given that there is a maximum of $\sim 1\%$ difference between these simulations, resolution seems to become a subdominant effect in our simulations once we reach $\sim 2 - 4$ cells

Table 3.3: Resolution dependence of key quantities for our fiducial models. Columns from left to right show model name, EOS used in `GR1D`, spatial resolution ($\Delta r/r = \{4.5, 1.1, 0.6\} \times 10^{-3}$ corresponds to $\{512, 2048, 4096\}$ cells per decade in radius in a logarithmic grid), mass ejected in the `FLASH` run $M_{\rm ej}$, and the total energy of ejecta in the `FLASH` run $E_{\rm ej}$.

Model	EOS	$\Delta r/r$ (10^{-3})	$M_{\rm ej}$ ($M_\odot$)	$E_{\rm ej}$ (10^{47} erg)
R15S1	SFHo	4.5	2.20	-0.130
R15S1		1.1	2.19	-0.119
R15D1	DD2	4.5	3.38	0.498
R15D1		1.1	3.37	0.489
			$M_{\rm ej}$ ($10^{-2}\,{\rm M}_\odot$)	
B25S1	SFHo	4.5	2.90	0.491
B25S1		1.1	2.80	0.399
B25D1	DD2	4.5	5.46	1.77
B25D1		1.1	5.45	1.76
			$M_{\rm ej}$ ($10^{-4}\,{\rm M}_\odot$)	
W40S1	SFHo	4.5	1.32	0.059
W40S1		0.6	1.44	0.067
W40D1	DD2	4.5	6.15	0.308
W40D1		0.6	6.30	0.326

per scale height. At that resolution, the surface pressure scale height seems to be resolved.

For the WR models, F18 obtained $\sim$ 0.3 cells per scale height at their highest resolution. In comparison, our "8X" results have a resolution of $\sim$ 3 cells per scale height. So, we expected that increasing the resolution for the WR models would yield a significant improvement numerically. Now that the surface pressure scale height is being resolved in the WR models, we believe that further increasing the resolution would yield similar results as in the RSG and BSG results; on the order of $\sim 1\%$ difference or less.

3.5 Implications for electromagnetic counterparts

Given the set-up of our simulations, we expected the ejection of the shock to generate electromagnetic emission in the form of shock breakout (Piro, 2013) and plateau emission (Lovegrove and Woosley, 2013). Our RSG plateau emission results are consistent with the failed supernova candidate NGC6946-BH1 found by Adams et al. (2017). The rest of the electromagnetic emission results were expected to vary widely for the BSGs and WRs (F18).

We estimate the shock breakout and plateau emission from failed SNe with the analytic formulae below. Table 3.4 shows these predictions for our three fiducial progenitors evolved with Mode 1 (Interpolation), using the DD2 and SFHo EOS to bracket the range in behavior. These predictions assume a spherically symmetric shock breakout and a recombination powered emission.

The shock breakout luminosity is given by (Piro, 2013)

$$L_{\rm bo} \simeq \frac{E_{\rm rad}}{\max(t_{\rm lc}, t_{\rm diff})}, \tag{3.6}$$

where $t_{\rm lc} = R_{\rm cc}/c$ is the light-crossing time over the stellar radius and

$$t_{\rm diff} = \tau_{\rm bo}\left(\frac{R_{\rm cc} - R_{\rm bo}}{c}\right) \tag{3.7}$$

is the radiation diffusion time, and $R_{\rm bo}$ is the stellar radius at which the optical depth $\tau_{\rm bo} = c/v_{\rm bo}$. The shock breakout velocity is set to the analytic value from Waxman and Katz (2017) of

$$v_{\rm bo} \simeq v_* \times \begin{cases} 13\, M_{\rm ej,10}^{0.16}\, v_{*,8.5}^{0.16}\, R_{\rm cc,12}^{-0.32} & \text{(BSG, WR)} \\ 4.5\, M_{\rm ej,10}^{0.13}\, v_{*,8.5}^{0.13}\, R_{\rm cc,12}^{-0.26} & \text{(RSG),} \end{cases} \tag{3.8}$$

where $v_* = \sqrt{E_{\rm ej}/M_{\rm ej}}$, $M_{\rm ej,10} = M/(10M_\odot)$, $v_{*,8.5} = v_*/(10^{8.5}\,{\rm cm\,s^{-1}})$, and $R_{\rm cc,12} = R_{\rm cc}/(10^{12}\,{\rm cm})$. The values of $v_{\rm bo}$ are shown for all fiducial progenitors using the SFHo and DD2 EOSs in Table 3.3, except for model R15S1, which has bound ejecta ($E_{\rm ej} < 0$). For WRs, the radiation energy in the breakout layer $E_{\rm rad}$ is obtained using Equation 31 of Waxman and Katz (2017), while for BSGs and RSGs it is measured directly from the simulation, where

$$E_{\rm rad} = \int aT^4 dV \tag{3.9}$$

over the shock at the time when $r_{\rm s} = R_{\rm cc}$. The temperature of the breakout emission is estimated using the luminosity and stellar radius,

$$L_{\rm bo} = 4\pi R_{\rm cc}^2\, \sigma T_{\rm bo}^4\ . \tag{3.10}$$

Plateau emission is estimated using the formulae of Kleiser and Kasen (2014), assuming a hydrogen recombination temperature of $10^4\,{\rm K}$ for RSGs and WRs, and $6\times10^3\,{\rm K}$ for BSGs given their surface composition, and an opacity $\kappa = 0.4\,{\rm cm^2\,g^{-1}}$ (F18).

Table 3.4: Bolometric shock breakout and plateau emission for our fiducial progenitors evolved with Mode 1 (Interpolation) and the DD2/SFHo EOSs. Columns from left to right show: model name, shock breakout luminosity $L_{\rm bo}$, breakout time $t_{\rm bo}$, shock velocity at breakout $v_{\rm bo}$, effective temperature at breakout $T_{\rm bo}$, plateau luminosity $L_{\rm pl}$, plateau duration $t_{\rm pl}$, and final shock velocity $v_{\rm exp}$. For reference, the pre-supernova luminosities are $\{1.3, 3.8, 5.7\} \times 10^5 L_\odot$ for models R15, B25, and W40, respectively.

Model	$L_{\rm bo}$ ($10^6\,{\rm L}_\odot$)	$t_{\rm bo}$	$v_{\rm bo}$ ($\rm km\,s^{-1}$)	$T_{\rm bo}$ ($10^4\,\rm K$)	$L_{\rm pl}$ ($10^5\,{\rm L}_\odot$)	$t_{\rm pl}$ (d)	$v_{\rm exp}$ ($\rm km\,s^{-1}$)
R15D1	2	8 d	40	0.6	2	400	40
B25S1	50	6 h	500	5	9	20	400
B25D1	300	3 h	900	8	20	20	600
W40S1	400	1 s	9,600	140	0.3	1	2,000
W40D1	600	1 s	13,000	150	0.6	2	2,000

The characteristic expansion velocity is

$$v_{\rm exp} = \sqrt{\frac{2E_{\rm ej}}{M_{\rm ej}}}\ . \tag{3.11}$$

Shock breakout in the RSG using the SFHo EOS can reach peak breakout luminosities $\sim 6 \times 10^{39}\,\rm erg\ s^{-1}$ ($\sim 10^6\,{\rm L}_\odot$) and last approximately 4 days. Compared to that, the model using the DD2 EOS can reach more than twice that peak luminosity and last for double the time ($2 \times 10^6\,{\rm L}_\odot$ for 8 days). The plateau emission for the R15S1 model is lower and longer ($10^5\,{\rm L}_\odot$ for 900 days) than R15D1 ($3 \times 10^5\,{\rm L}_\odot$ for 500 days). These values are still consistent with the estimates of Piro (2013) and Lovegrove et al. (2017). With a temperature of $\rm T_{bo} \approx 6000\,K$ for the SFHo case or up to $\approx 10000\,\rm K$ for the DD2 case, we expect the ionization of hydrogen and the further recombination to be a strong optical signature of this progenitor.

The BSG progenitor with the SFHo EOS reaches a peak breakout luminosity of $\sim 3 \times 10^{41}\,\rm erg\ s^{-1}$ ($\sim 8 \times 10^7\ {\rm L}_\odot$) with a duration of about 6 hours. In comparison, the BSG progenitor with the DD2 EOS reaches about 4 times the peak luminosity ($\sim 3 \times 10^8\ {\rm L}_\odot$) for roughly a third of the time, about 2 hours.

The plateau emission for the B25S1 model is lower (9×10^5 $L_\odot$) than for the B25D1 model (2.5×10^6 $L_\odot$) for the same amount of time — about 20 days. The temperature for these models is relatively similar and so these progenitors remain good candidates for wide-field, short-cadence surveys. The plateau estimates are slightly different than those of F18: the plateau luminosity is about 2x larger and roughly for the same duration. A breakout luminosity of $\sim 10^{41}$ erg s^{-1} would be easily detectable (for example, with SWIFT, with cadence and depth corresponding to values presented in Table 3.4), as well as the plateau luminosity of $\sim 10^{40}$ erg s^{-1} with a duration of approximately several weeks.

The resulting breakout luminosity in the W40S1 model, $\sim 2 \times 10^{42}$ erg s^{-1} ($\sim 4 \times 10^8$ $L_\odot$), is roughly the same as in F18, the breakout luminosity in the W40D1 model is about double ($\sim 6 \times 10^8$ $L_\odot$). We found the energy density $E_{\rm rad,bo}$ contained within the shock to be similar to the energy imparted onto the shock in the BSG and RSG cases, however the diffusion time was smaller than the light-crossing time, which was about one second. For the plateau estimates, we expect $L_{\rm pl} \approx 10^{38}$ erg s^{-1} $= 3 \times 10^4$ $L_\odot$ for about one or two days, which is fainter than the presupernova luminosity for the WR case, like in F18. This transient event should occur in the high UV, low X-ray regime with a temperature of $T_{\rm bo} \approx 10^6$ K, though this emission would be highly dependent on the ambient medium and the evolution history of the progenitor (WR's are known for strong stellar winds before core collapse and a denser ambient medium would serve to further obscure any optical emission from the ejected shock).

Overall, it seems that most of the observational predictions of F18 remain roughly consistent with the stiff EOS case, as was implied from previous sections. In the cases with the soft EOS, we observe the pattern of lower energies and observational signatures overall. While some quantities may be sensitive to the details of the shock velocity, as well as the ambient medium if the shock

escapes, the general pattern seems to hold. In the context of optical transient surveys, the most promising signatures remain the cases of shock breakout in RSGs and plateau emission in BSGs, both of which have durations on the order of days and bolometric luminosities of $10^{39}\,\mathrm{erg\,s^{-1}}$. Shock breakout from BSGs is also a good candidate for surveys with hour-long cadences and UV capabilities.

Chapter 4

Summary and Discussion

We have studied mass ejection in failed core-collapse supernovae driven by neutrino losses, by incorporating a general relativistic approach in handling the inner core evolution of collapsing massive stars. During the protoneutron star phase, some gravitational mass-energy is lost through neutrinos. This change in gravitational mass is felt instantaneously at radii $\gtrsim 10^9\,\mathrm{cm}$. The over-pressurized material at those radii develops into an outward sound pulse that steepens into a shock. For most progenitors, this shock makes it out of the star. We use time-dependent hydrodynamic simulations to track this shock throughout and outside the star and to quantitatively determine how much material is ejected and whether the ejected material is gravitationally bound or unbound. If the material is unbound, we make observational predictions for the bolometric EM emission by the ejected material. Our main results are the following:

1. Using the general relativistic code `GR1D` to compute the neutrino mass loss as a function of time and including the result in our time-dependent hydrodynamic simulations in `FLASH` allowed us to calculate the mass and energy ejecta self-consistently for all the tested progenitors. Quantitatively, our results match those of F18 when we use a stiff EOS (DD2), while the ejecta masses and energies are several times smaller in the soft

EOS case (SFHo). (Figure 3.1)

2. We find that using a linear analytic ramp function to define the neutrino mass loss provides us with results that are $\sim 20\%$ different for the WR cases and $\sim 5\%$ different in the RSG and BSG cases compared to using the full neutrino mass loss history from `GR1D`. The linear ramp requires only three parameters ($t_{\rm stall}$, $t_{\rm bh}$, and $\delta M_{\rm G}$), which we obtain from the `GR1D` simulations (Figure 3.6), and are easily obtainable from other published SN simulations.

3. Spatial resolution plays an important role in the WR simulations, where the surface pressure scale height was not resolved in F18. In those cases, the difference in ejecta energy and mass was on the order of $\sim 20\%$, while in the well-resolved RSG and BSG cases, increasing the resolution only amounted to $\sim 1\%$ difference in the results (Table 3.3).

4. In all models in which we remapped the domain from `GR1D` into `FLASH`, there was a few percent discrepancy in the enclosed baryonic mass at the mapping radius. This resulted in none of our fiducial progenitors ejecting any mass. So, we include this mode of evolution in the work as a reference, despite the fact that the results are unreliable due to this discrepancy. (Table 3.1)

5. The observational predictions of F18 for shock breakout and plateau emission remain consistent with the stiff DD2 EOS case, while those with the soft SFHo EOS are several times fainter (Table 3.4). Shock breakouts from RSG models remain promising candidates for detection by optical transient surveys together with plateau emission from BSG models, both of which have durations on the order of days and bolometric luminosities of $10^{39}\,{\rm erg\,s^{-1}}$.

Consistent with previous work, we recover several key trends. First is an inverse trend between the ejected mass and envelope compactness (Figure 3.2, bottom right). This is related to the fact that given shock energies of a characteristic magnitude, the mass ejected is inverse proportional to the surface gravity of the star. Second, the gravitational mass lost to neutrino emission follows a monotonically decreasing trend with core compactness in Figure 3.3, which is representative of an inverse dependence of the ejecta energy on core compactness (Figure 3.2, top left). Higher compactness is associated with a shorter time to BH formation (O'Connor and Ott, 2010; da Silva Schneider et al., 2020), which results in less mass-energy lost to neutrinos. Lastly, ejecta energy shows a weak trend with envelope compactness (Figure 3.2, top right), but energy per unit mass (and hence velocity) of the ejecta shows a strong trend with the envelope compactness (Figure 3.4).

Our predictions can be improved upon in several ways. Quantitatively, while DD2 and SFHo are consistent with experimental and observational constraints and unitary gas bounds on the symmetry energy and its density derivative, LS220 is not (Tews et al., 2017). Adding more EOSs covering the range of plausible EOSs would improve our results the most. Using improved observational constraints for the NS radius from LIGO or NICER to narrow down the EOS range will yield a narrower range of predictions for electromagnetic emission. Our uncertainty in the ejecta energy and mass are highest with respect to EOS, but the second highest source of error is using `GR1D` Version 1 versus Version 2, which differ in the accuracy of their neutrino transport. We find that the difference of $\delta M_{\rm G}$ at the point where Version 2 fails to converge is on the order of $\sim 20\%$ (see Appendix C). Lastly, using the simplicity of the neutrino mass loss history, further work could be done in which the analytic ramp is used for a much larger population of progenitors to densely populate the parameter spaces explored in Chapter 3.

Bibliography

S. M. Adams, C. S. Kochanek, J. R. Gerke, K. Z. Stanek, and X. Dai. The search for failed supernovae with the Large Binocular Telescope: confirmation of a disappearing star. *MNRAS*, 468(4):4968–4981, Jul 2017. doi: 10.1093/mnras/stx816.

W. Baade and F. Zwicky. Remarks on Super-Novae and Cosmic Rays. *Physical Review*, 46(1):76–77, July 1934a. doi: 10.1103/PhysRev.46.76.2.

W. Baade and F. Zwicky. Cosmic Rays from Super-novae. *Proceedings of the National Academy of Science*, 20(5):259–263, May 1934b. doi: 10.1073/pnas.20.5.259.

W. Baade and F. Zwicky. On Super-novae. *Proceedings of the National Academy of Science*, 20(5):254–259, May 1934c. doi: 10.1073/pnas.20.5.254.

C. M. Basinger, C. S. Kochanek, S. M. Adams, X. Dai, and K. Z. Stanek. The Search for Failed Supernovae with the Large Binocular Telescope: N6946-BH1, Still No Star. *arXiv e-prints*, art. arXiv:2007.15658, July 2020.

Christian Y. Cardall, Eirik Endeve, and Anthony Mezzacappa. Conservative 3+1 general relativistic variable Eddington tensor radiation transport equations. *PhRvD*, 87(10):103004, May 2013. doi: 10.1103/PhysRevD.87.103004.

P. Colella and P. R. Woodward. The Piecewise Parabolic Method (PPM) for Gas-Dynamical Simulations. *JCP*, 54:174–201, September 1984.

Stirling A. Colgate and Richard H. White. The Hydrodynamic Behavior of Supernovae Explosions. *ApJ*, 143:626, March 1966. doi: 10.1086/148549.

Sean M. Couch and Christian D. Ott. The Role of Turbulence in Neutrino-driven Core-collapse Supernova Explosions. *ApJ*, 799(1):5, January 2015. doi: 10.1088/0004-637X/799/1/5.

Sean M. Couch, Emmanouil Chatzopoulos, W. David Arnett, and F. X. Timmes. The Three-dimensional Evolution to Core Collapse of a Massive Star. *ApJL*, 808(1):L21, July 2015. doi: 10.1088/2041-8205/808/1/L21.

Eric R. Coughlin, Eliot Quataert, Rodrigo Fernández, and Daniel Kasen. A physical model of mass ejection in failed supernovae. *MNRAS*, 477(1):1225–1238, Jun 2018a. doi: 10.1093/mnras/sty667.

Eric R. Coughlin, Eliot Quataert, and Stephen Ro. Weak Shock Propagation with Accretion. I. Self-similar Solutions and Application to Failed Supernovae. *ApJ*, 863(2):158, Aug 2018b. doi: 10.3847/1538-4357/aad198.

Eric R. Coughlin, Stephen Ro, and Eliot Quataert. Weak Shock Propagation with Accretion. II. Stability of Self-similar Solutions to Radial Perturbations. *ApJ*, 874(1):58, Mar 2019. doi: 10.3847/1538-4357/ab09ec.

André da Silva Schneider, Evan O'Connor, Elvira Granqvist, Aurore Betranhandy, and Sean M. Couch. Equation of State and Progenitor Dependence of Stellar-mass Black Hole Formation. *ApJ*, 894(1):4, May 2020. doi: 10.3847/1538-4357/ab8308.

Anshu Dubey, Katie Antypas, Murali K. Ganapathy, Lynn B. Reid, Katherine Riley, Dan Sheeler, Andrew Siegel, and Klaus Weide. Extensible component-based architecture for flash, a massively parallel, multiphysics simulation code. *J. Par. Comp.*, 35(10-11): 512 – 522, 2009. ISSN 0167-8191. doi: DOI:10.1016/j.parco.

2009.08.001. URL http://www.sciencedirect.com/science/article/B6V12-4X54JHJ-1/2/b261a63ad1957b89222e859101236ca7.

T. Ertl, H.-T. Janka, S. E. Woosley, T. Sukhbold, and M. Ugliano. A Two-parameter Criterion for Classifying the Explodability of Massive Stars by the Neutrino-driven Mechanism. *ApJ*, 818:124, February 2016. doi: 10.3847/0004-637X/818/2/124.

Rodrigo Fernández. Hydrodynamics of Core-collapse Supernovae at the Transition to Explosion. I. Spherical Symmetry. *ApJ*, 749(2):142, Apr 2012. doi: 10.1088/0004-637X/749/2/142.

Rodrigo Fernández, Eliot Quataert, Kazumi Kashiyama, and Eric R. Coughlin. Mass ejection in failed supernovae: variation with stellar progenitor. *MNRAS*, 476(2):2366–2383, May 2018. doi: 10.1093/mnras/sty306.

C. L. Fryer, S. E. Woosley, and A. Heger. Pair-Instability Supernovae, Gravity Waves, and Gamma-Ray Transients. *ApJ*, 550(1):372–382, March 2001. doi: 10.1086/319719.

B. Fryxell, K. Olson, P. Ricker, F. X. Timmes, M. Zingale, D. Q. Lamb, P. MacNeice, R. Rosner, J. W. Truran, and H. Tufo. FLASH: An Adaptive Mesh Hydrodynamics Code for Modeling Astrophysical Thermonuclear Flashes. *ApJS*, 131:273–334, November 2000. doi: 10.1086/317361.

B. A Fryxell, E. Müller, and D. Arnett. Hydrodynamics and Nuclear Burning. *MPI Astrophys. Rep.*, 449, November 1989. doi: 10.1086/317361.

J. R. Gerke, C. S. Kochanek, and K. Z. Stanek. The search for failed supernovae with the Large Binocular Telescope: first candidates. *MNRAS*, 450(3):3289–3305, July 2015. doi: 10.1093/mnras/stv776.

Annastasia Haynie and Anthony L Piro. Shock Breakout in Dense Circumstellar Material with Application to PS1-13arp. *arXiv e-prints*, art. arXiv:2011.01937, November 2020.

M. Hempel, T. Fischer, J. Schaffner-Bielich, and M. Liebendörfer. New Equations of State in Simulations of Core-collapse Supernovae. *ApJ*, 748:70, March 2012. doi: 10.1088/0004-637X/748/1/70.

Hans-Thomas Janka. *Neutrino-Driven Explosions*, page 1095. Alsabti, Athem W. and Murdin, Paul, 2017. doi: 10.1007/978-3-319-21846-5_109.

Hans-Thomas Janka, Tobias Melson, and Alexander Summa. Physics of Core-Collapse Supernovae in Three Dimensions: A Sneak Preview. *Annual Review of Nuclear and Particle Science*, 66(1):341–375, October 2016. doi: 10.1146/annurev-nucl-102115-044747.

Daniel Kasen, S. E. Woosley, and Alexander Heger. Pair Instability Supernovae: Light Curves, Spectra, and Shock Breakout. *ApJ*, 734(2):102, June 2011. doi: 10.1088/0004-637X/734/2/102.

B. Katz, N. Sapir, and E. Waxman. X-rays, γ-rays and neutrinos from collisionless shocks in supernova wind breakouts. In P. Roming, N. Kawai, and E. Pian, editors, *Death of Massive Stars: Supernovae and Gamma-Ray Bursts*, volume 279 of *IAU Symposium*, pages 274–281, September 2012. doi: 10.1017/S174392131201304X.

I. K. W. Kleiser and D. Kasen. Rapidly fading supernovae from massive star explosions. *MNRAS*, 438:318–328, February 2014. doi: 10.1093/mnras/stt2191.

Christopher S. Kochanek, John F. Beacom, Matthew D. Kistler, José L. Prieto, Krzysztof Z. Stanek, Todd A. Thompson, and Hasan Yüksel. A Survey About

Nothing: Monitoring a Million Supergiants for Failed Supernovae. *ApJ*, 684 (2):1336–1342, Sep 2008. doi: 10.1086/590053.

K. Langanke and G. Martínez-Pinedo. Shell-model calculations of stellar weak interaction rates: II. Weak rates for nuclei in the mass range /A=45-65 in supernovae environments. *Nuc. Phys. A*, 673(1-4):481–508, Jun 2000. doi: 10.1016/S0375-9474(00)00131-7.

K. Langanke, G. Martínez-Pinedo, J. M. Sampaio, D. J. Dean, W. R. Hix, O. E. Messer, A. Mezzacappa, M. Liebendörfer, H. Th. Janka, and M. Rampp. Electron Capture Rates on Nuclei and Implications for Stellar Core Collapse. *PRL*, 90(24):241102, Jun 2003. doi: 10.1103/PhysRevLett.90.241102.

J. M. Lattimer and F. D. Swesty. A generalized equation of state for hot, dense matter. *Nuclear Physics A*, 535:331–376, December 1991. doi: 10.1016/0375-9474(91)90452-C.

M. Liebendörfer, A. Mezzacappa, F.-K. Thielemann, O. E. Messer, W. R. Hix, and S. W. Bruenn. Probing the gravitational well: No supernova explosion in spherical symmetry with general relativistic Boltzmann neutrino transport. *PRD*, 63(10):103004–+, May 2001.

Matthias Liebendörfer. A Simple Parameterization of the Consequences of Deleptonization for Simulations of Stellar Core Collapse. *ApJ*, 633(2):1042–1051, Nov 2005. doi: 10.1086/466517.

E. Lovegrove and S. E. Woosley. Very Low Energy Supernovae from Neutrino Mass Loss. *ApJ*, 769:109, June 2013. doi: 10.1088/0004-637X/769/2/109.

E. Lovegrove, S. E. Woosley, and W. Zhang. Very Low Energy Supernovae: Light Curves and Spectra of Shock Breakout. *ApJ, submitted, arXiv:1706.02240*, June 2017.

A. I. MacFadyen and S. E. Woosley. Collapsars: Gamma-Ray Bursts and Explosions in "Failed Supernovae". *ApJ*, 524(1):262–289, October 1999. doi: 10.1086/307790.

Tobias Melson, Hans-Thomas Janka, Robert Bollig, Florian Hanke, Andreas Marek, and Bernhard Müller. Neutrino-driven Explosion of a 20 Solar-mass Star in Three Dimensions Enabled by Strange-quark Contributions to Neutrino-Nucleon Scattering. *ApJL*, 808(2):L42, August 2015. doi: 10.1088/2041-8205/808/2/L42.

G. N. Minerbo. Maximum entropy Eddington factors. *J. Quant. Sp. & Rad. Tr.*, 20(6):541–545, Jan 1978. doi: 10.1016/0022-4073(78)90024-9.

Bernhard Müller, Alexander Heger, David Liptai, and Joshua B. Cameron. A simple approach to the supernova progenitor-explosion connection. *MNRAS*, 460(1):742–764, Jul 2016a. doi: 10.1093/mnras/stw1083.

Bernhard Müller, Maxime Viallet, Alexander Heger, and Hans-Thomas Janka. The Last Minutes of Oxygen Shell Burning in a Massive Star. *ApJ*, 833(1): 124, December 2016b. doi: 10.3847/1538-4357/833/1/124.

D. K. Nadyozhin. Some secondary indications of gravitational collapse. *Ap&SS*, 69:115–125, May 1980. doi: 10.1007/BF00638971.

E. O'Connor and C. D. Ott. Black Hole Formation in Failing Core-Collapse Supernovae. *ApJ*, 730:70, April 2011. doi: 10.1088/0004-637X/730/2/70.

Evan O'Connor. An Open-source Neutrino Radiation Hydrodynamics Code for Core-collapse Supernovae. *ApJS*, 219(2):24, Aug 2015. doi: 10.1088/0067-0049/219/2/24.

Evan O'Connor and Christian D. Ott. A new open-source code for spherically symmetric stellar collapse to neutron stars and black holes. *Classical and*

Quantum Gravity, 27(11):114103, Jun 2010. doi: 10.1088/0264-9381/27/11/114103.

Evan O'Connor et al. Global comparison of core-collapse supernova simulations in spherical symmetry. *Journal of Physics G Nuclear Physics*, 45(10):104001, Oct 2018. doi: 10.1088/1361-6471/aadeae.

T. Oda, M. Hino, K. Muto, M. Takahara, and K. Sato. Rate Tables for the Weak Processes of sd-Shell Nuclei in Stellar Matter. *Atomic Data and Nuclear Data Tables*, 56(2):231–403, Mar 1994. doi: 10.1006/adnd.1994.1007.

Kuo-Chuan Pan, Matthias Liebendörfer, Sean M. Couch, and Friedrich-Karl Thielemann. Equation of State Dependent Dynamics and Multi-messenger Signals from Stellar-mass Black Hole Formation. *ApJ*, 857(1):13, Apr 2018. doi: 10.3847/1538-4357/aab71d.

Bill Paxton, Lars Bildsten, Aaron Dotter, Falk Herwig, Pierre Lesaffre, and Frank Timmes. Modules for Experiments in Stellar Astrophysics (MESA). *ApJS*, 192(1):3, Jan 2011. doi: 10.1088/0067-0049/192/1/3.

Bill Paxton, Matteo Cantiello, Phil Arras, Lars Bildsten, Edward F. Brown, Aaron Dotter, Christopher Mankovich, M. H. Montgomery, Dennis Stello, F. X. Timmes, and Richard Townsend. Modules for Experiments in Stellar Astrophysics (MESA): Planets, Oscillations, Rotation, and Massive Stars. *ApJS*, 208(1):4, Sep 2013. doi: 10.1088/0067-0049/208/1/4.

Bill Paxton, Pablo Marchant, Josiah Schwab, Evan B. Bauer, Lars Bildsten, Matteo Cantiello, Luc Dessart, R. Farmer, H. Hu, N. Langer, R. H. D. Townsend, Dean M. Townsley, and F. X. Timmes. Modules for Experiments in Stellar Astrophysics (MESA): Binaries, Pulsations, and Explosions. *ApJS*, 220(1):15, Sep 2015. doi: 10.1088/0067-0049/220/1/15.

Bill Paxton, Josiah Schwab, Evan B. Bauer, Lars Bildsten, Sergei Blinnikov,

Paul Duffell, R. Farmer, Jared A. Goldberg, Pablo Marchant, Elena Sorokina, Anne Thoul, Richard H. D. Townsend, and F. X. Timmes. Modules for Experiments in Stellar Astrophysics (MESA): Convective Boundaries, Element Diffusion, and Massive Star Explosions. *ApJS*, 234(2):34, Feb 2018. doi: 10.3847/1538-4365/aaa5a8.

Bill Paxton, R. Smolec, Josiah Schwab, A. Gautschy, Lars Bildsten, Matteo Cantiello, Aaron Dotter, R. Farmer, Jared A. Goldberg, Adam S. Jermyn, S. M. Kanbur, Pablo Marchant, Anne Thoul, Richard H. D. Townsend, William M. Wolf, Michael Zhang, and F. X. Timmes. Modules for Experiments in Stellar Astrophysics (MESA): Pulsating Variable Stars, Rotation, Convective Boundaries, and Energy Conservation. *ApJS*, 243(1):10, July 2019. doi: 10.3847/1538-4365/ab2241.

A. L. Piro. Taking the "Un" out of "Unnovae". *ApJL*, 768:L14, May 2013. doi: 10.1088/2041-8205/768/1/L14.

M. Rampp and H.-T. Janka. Radiation hydrodynamics with neutrinos. Variable Eddington factor method for core-collapse supernova simulations. *A&A*, 396: 361–392, December 2002. doi: 10.1051/0004-6361:20021398.

Stephen Ro, Eric R. Coughlin, and Eliot Quataert. Weak Shock Propagation with Accretion. III. A Numerical Study On Shock Propagation & Stability. *submitted, arXiv:1904.01706*, art. arXiv:1904.01706, Apr 2019.

Jose V. Romero, Jose M. A. Ibanez, Jose M. A. Marti, and Juan A. Miralles. A New Spherically Symmetric General Relativistic Hydrodynamical Code. *ApJ*, 462:839, May 1996. doi: 10.1086/177198.

S. Rosswog and M. Liebendörfer. High-resolution calculations of merging neutron stars - II. Neutrino emission. *MNRAS*, 342(3):673–689, Jul 2003. doi: 10.1046/j.1365-8711.2003.06579.x.

A. S. Schneider, L. F. Roberts, C. D. Ott, and E. O'Connor. Equation of state effects in the core collapse of a 20Msun star. *PRC*, 100(5):055802, November 2019. doi: 10.1103/PhysRevC.100.055802.

S. J. Smartt, J. J. Eldridge, R. M. Crockett, and J. R. Maund. The death of massive stars - I. Observational constraints on the progenitors of Type II-P supernovae. *MNRAS*, 395(3):1409–1437, May 2009. doi: 10.1111/j.1365-2966.2009.14506.x.

A. W. Steiner, M. Hempel, and T. Fischer. Core-collapse Supernova Equations of State Based on Neutron Star Observations. *ApJ*, 774:17, September 2013. doi: 10.1088/0004-637X/774/1/17.

T. Sukhbold and S. E. Woosley. The Compactness of Presupernova Stellar Cores. *ApJ*, 783:10, March 2014. doi: 10.1088/0004-637X/783/1/10.

Chris Sullivan, Evan O'Connor, Remco G. T. Zegers, Thomas Grubb, and Sam M. Austin. The Sensitivity of Core-collapse Supernovae to Nuclear Electron Capture. *ApJ*, 816(1):44, Jan 2016. doi: 10.3847/0004-637X/816/1/44.

K. Sumiyoshi, S. Yamada, H. Suzuki, H. Shen, S. Chiba, and H. Toki. Post-bounce Evolution of Core-Collapse Supernovae: Long-Term Effects of the Equation of State. *ApJ*, 629:922–932, August 2005. doi: 10.1086/431788.

Ingo Tews, James M. Lattimer, Akira Ohnishi, and Evgeni E. Kolomeitsev. Symmetry Parameter Constraints from a Lower Bound on Neutron-matter Energy. *ApJ*, 848(2):105, Oct 2017. doi: 10.3847/1538-4357/aa8db9.

T. A. Thompson, A. Burrows, and P. A. Pinto. Shock Breakout in Core-Collapse Supernovae and Its Neutrino Signature. *ApJ*, 592:434–456, July 2003. doi: 10.1086/375701.

F. X. Timmes and F. Douglas Swesty. The Accuracy, Consistency, and Speed of an Electron-Positron Equation of State Based on Table Interpolation of the Helmholtz Free Energy. *ApJS*, 126(2):501–516, Feb 2000. doi: 10.1086/313304.

M. Ugliano, H.-T. Janka, A. Marek, and A. Arcones. Progenitor-explosion Connection and Remnant Birth Masses for Neutrino-driven Supernovae of Iron-core Progenitors. *ApJ*, 757:69, September 2012. doi: 10.1088/0004-637X/757/1/69.

Trevor Vincent, Francois Foucart, Matthew D. Duez, Roland Haas, Lawrence E. Kidder, Harald P. Pfeiffer, and Mark A. Scheel. Unequal Mass Binary Neutron Star Simulations with Neutrino Transport: Ejecta and Neutrino Emission. *arXiv:1908.00655*, art. arXiv:1908.00655, Aug 2019.

Eli Waxman and Boaz Katz. Shock Breakout Theory. In Athem W. Alsabti and Paul Murdin, editors, *Handbook of Supernovae*, page 967, 2017. doi: 10.1007/978-3-319-21846-5_33.

James R. Wilson. Supernovae and Post-Collapse Behavior. In *Numerical Astrophysics*, page 422, January 1985.

S. E. Woosley and A. Heger. Nucleosynthesis and remnants in massive stars of solar metallicity. *Phys. Rep.*, 442(1-6):269–283, Apr 2007. doi: 10.1016/j.physrep.2007.02.009.

Appendix A

GR1D verification tests

GR1D is an open-source general-relativistic spherically-symmetric neutrino radiation hydrodynamics code developed by O'Connor and Ott (2010). Its intended purpose is for the evolution of stars from collapse to neutron stars or black holes. GR1D was used to simulate the inner core evolution in all the progenitors listed in Table 3.1 and Table D.1. To generate trust in the results of the GR1D simulations, we completed some verification tests. First, we tested if GR1D can properly simulate the behaviour of a simple hydrodynamic case — the Sedov blast. Since we know the analytic solution to this case, we can quantify how closely the code reproduces it and therefore discuss errors in simulating other hydrodynamic cases. Secondly, we use a more specific verification test — a core collapse. This is done to verify that we are using GR1D as intended by assessing the degree to which we can reproduce the core collapse simulation put forth as a test in O'Connor and Ott (2010).

A.1 Sedov Blast

The Sedov blast is widely used as a test case for hydrodynamic codes. A large amount of energy is deposited in a small, localized volume in the center of the simulation domain. A shock wave is generated that should expand

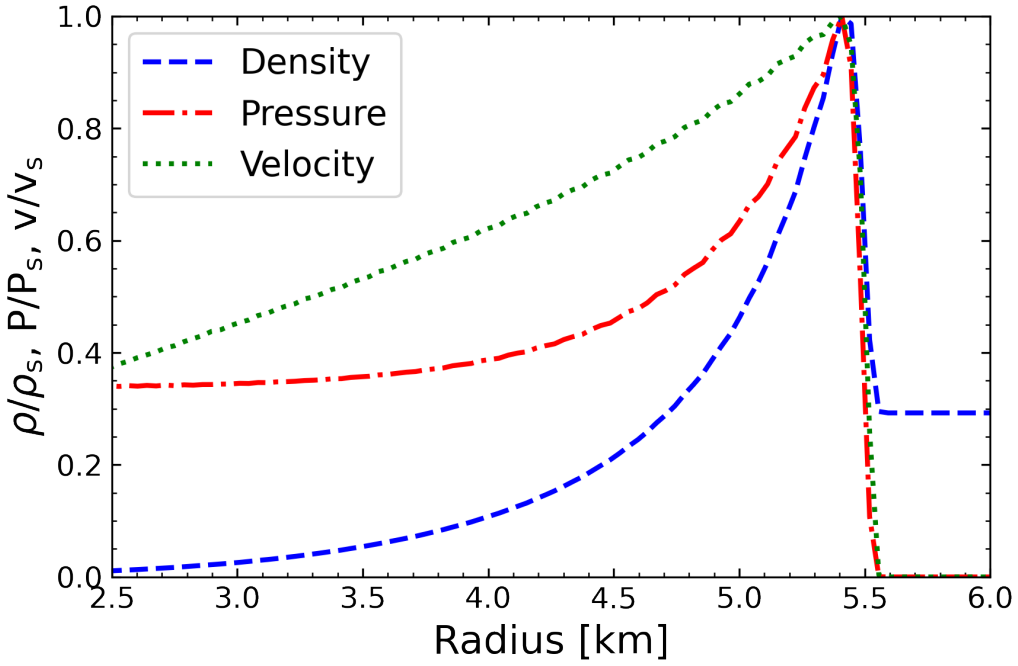

Figure A.1: The Sedov blast wave problem at t = 0.1s with the initial parameters described in O'Connor and Ott (2010). The numerical results of density, pressure, and velocity are normalized against their shock values at that time.

spherically outward into rest of the allotted space. We use this test because we know the analytic solution to it, which means that we can quantitatively test the hydrodynamic code to see how well it simulates a simple hydrodynamic case like this. We can use higher resolution simulations to test how well the simulation converges to the analytic solution.

We simulated a Sedov blast to high accuracy and compare it to the results presented in the tests to the code in O'Connor and Ott (2010). The domain and set-up used in generating this test case was the default provided with `GR1D`. In Figure A.1, the Sedov blast is shown at t= 0.1 s, the same time as in Fig. 2 of O'Connor and Ott (2010). We obtain the same general structure of the blast, as well as the same level of accuracy as in the original test case. Compared to the analytic solution shown in O'Connor and Ott (2010), we see slight off-sets in the simulated solution: the peaks of the shock are rounded-off (compared to the analytically expected sharp edge), and the leading edge of the shock is not

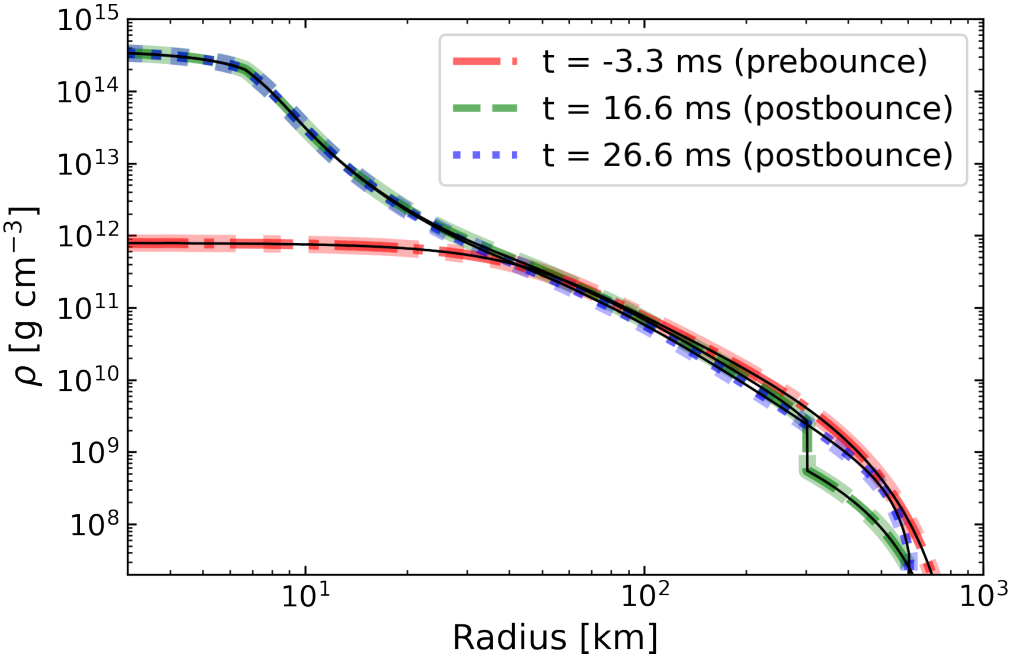

Figure A.2: Radial density profiles for core collapse simulations using the hybrid EOS in `GR1D`. The density profiles shown are for 3.3 ms prebounce (red dashed-dotted lines), 16.6 ms (green dashed lines), and 26.6 ms (blue dotted lines) postbounce. The highest resolution profiles for all times are all thin solid black lines.

a perfectly vertical edge. Realistically, no hydrodynamic code will perfectly match the analytic function, but what should (and does) happen is that the simulation should converge towards the analytic solution with increasing resolution. Despite the fact that we use a relatively low-resolution, `GR1D` reproduces the analytic solution at our desired accuracy.

A.2 Hybrid Collapse

Among the other verification tests presented in O'Connor and Ott (2010) that are useful, we also simulate the "Hybrid Core-Collapse: Converge" test case. We do this, because our work deals with simulating core-collapse supernovae, so running a core-collapse test means that we verify that our `GR1D` simulations

quantitatively match the expected outcome that the O'Connor and Ott (2010) obtain with the code.

A hybrid EOS is used to run three different core-collapse simulations: one using 500 radial zones, one with 1500, and the third with 4500. Using three different resolutions allows us to quantify the convergence of any given hydrodynamic quantity (they used M_{grav} in O'Connor and Ott (2010)) in the simulations versus the resolution used. In Figure A.2, we show the radial density profile for the core-collapse simulations at three times: 3.3 ms prebounce, 16.6 ms and 26.6 ms postbounce. At these three times, the thin black lines show the highest resolution simulations. The same convergence test was done in O'Connor and Ott (2010) (see Fig. 4 of their paper) and we obtain the same results. Achieving these identical results provides the necessary credibility for the results from the `GR1D` simulations in our work.

Appendix B

Tests of the FLASH setup

To confirm that the effect that we are studying is the one responsible for the results presented (e.g., M_{ej}, E_{ej}, observational properties), I completed some simulations with the fiducial progenitors where no neutrino mass-loss was present. I will refer to this case as Mode 0.

These simulations were completed using the exact same FLASH code used in our default case (Mode 1: Interpolation). The only difference in the simulations for Mode 0 compared to Mode 1 is that there is no neutrino mass loss, which means no shift in gravity, and therefore $M_{grav} = M_{bary}$. While we added Mode 1 as a functionality to FLASH for the purpose of this work and used it as the default method, as described in Section 2.4, Fernández et al. (2018) added Mode 0 (as I'm referring to it here) into this version of FLASH by Fernández et al. (2018) for the same purposes of testing the code versus the "control" case (the control being no gravitational mass lost).

In Fig. B.1, I plot the differences that arise between Mode 0 (dashed lines) and Mode 1 (solid lines) in terms of the evolution of the radial velocity and density. All simulations between the two modes were completed to the same t_{end} for consistency. The most obvious difference between the two is in the comparison of the velocities. For Mode 1, there is an obvious and sharp leading edge of a shock moving outwards with positive velocities in all three fiducial

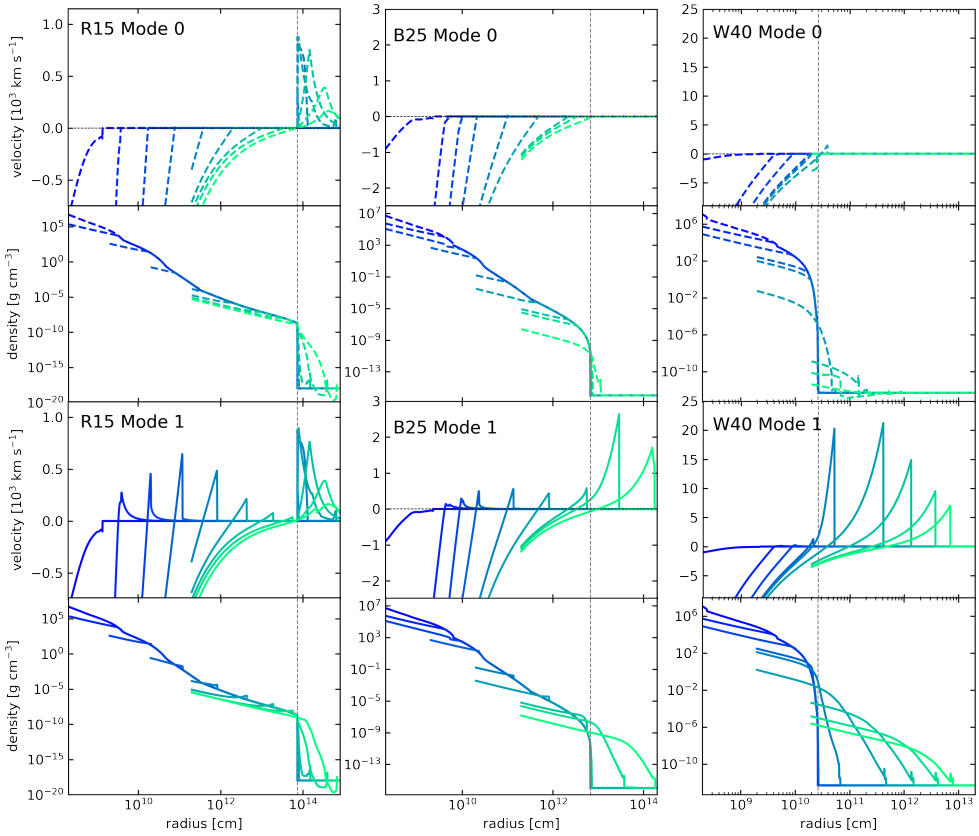

Figure B.1: The three columns are divided into the three fiducial progenitors. From left to right, they are the 15 $M_\odot$ RSG, the 25 $M_\odot$ BSG, and the 40 $M_\odot$ WR progenitors. The top two rows show the velocity and density evolution of the simulations for Mode 0 (dashed lines) and the bottom two rows for Mode 1 (solid lines). The colors in the plot represent different times of the simulation to show the progression of the simulation: blue at the beginning of the simulation and green at the end. The simulation times are roughly equally divided (logarithmically) and go from $t_{start} = 10$ seconds to $t_{end} = \{10^4, 10^6, 2\times10^7\}$ seconds for the {RSG,BSG,WR} progenitors. The thin vertical dashed grey line represents the radius of the respective star at core collapse.

progenitors, whereas no such case exists for Mode 0. In Mode 0, all the fiducial progenitors collapse to a BH without any material ever escaping the domain. The existence of this shock can also be seen in the differences between the density plots. In the Mode 1 simulations (fourth row), there is a "bump" that travels outwards and leaves the surface of the star. That is most easily seen for the 40 $M_\odot$ WR progenitor (bottom right panel), where it appears like a double dump until t_{end}.

In both the 25 $M_\odot$ BSG and 40 $M_\odot$ WR Mode 0 simulations, the star promptly collapses to a BH and no material within the domain of the star develops any positive velocity. As there is no ejecta from any of the Mode 0 simulations, then both of these stars would just disappear without any observational signatures.

In the RSG 15$M_\odot$ progenitor, it is evident from both modes that there is some material that develops positive velocity just outside the surface of the star, as can be seen in Fig. B.1, top two RSG panels. This is very low density material (Fig. B.1, bottom two RSG panels) that the star loses slowly after the start of the simulation for a number of potential reasons. Most likely, it is because we define the domain outside the surface of the star as a constant, very low ambient density, which introduces a very sharp gradient at the beginning of the simulation. This set-up leaves the ambient in an imperfect hydrostatic equilibrium, so when it is allowed to evolve hydrodynamically, ambient "fluff" appears near the surface of the star.

This low density, ambient material that develops outside the surface of the star occurs in both Mode 0 and Mode 1. So, to highlight the differences between the two modes, I remove the ambient material with positive velocity outside the star in Fig. B.2. This is done by creating a Boolean mask, defined as "True" below R_{cc} (anything inside the star) and "False" otherwise (anything outside the star). This allows my Python script that calculates all the hydrodynamic quantities to set all the ones outside the star to zero since we do not need to

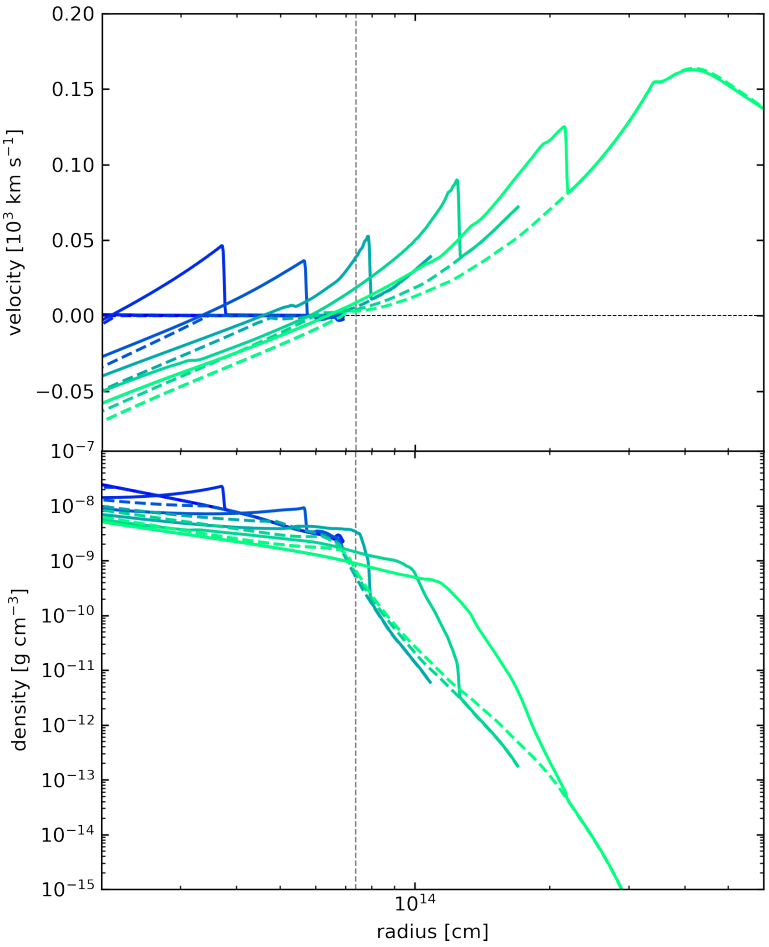

Figure B.2: A closer look at the difference between Mode 0 and Mode 1 for the 15 $M_\odot$ RSG progenitor. Both panels are a combination of both Mode 0 and Mode 1 to show the differences in a bit more detail. The top panel shows the evolution of the velocities and the bottom panel is the densities. The colors and lines are defined the same as in Fig. B.1. The times of the simulations presented are calculated at greater resolution and the ambient material that develops outside the evolution of the shock has been removed for greater clarity.

track them.

In Fig. B.2, the top panel is the evolution of the velocities and the bottom, the densities. Once the ambient material is removed, it is easy to see that the only difference between Mode 0 (dashed line) and Mode 1 (solid line) is that there is a shock, defined by the sharp leading edge (when $v > 0$ behind the leading edge) in the velocity plot. This shock can also be tracked in the density plot until it reaches the ambient medium outside the surface of the star, where it dissipates and expands.

Given that the only difference between the two modes is the inclusion of the neutrino mass-loss, this shock that gets ejected in all three fiducial progenitors is present due to the difference between the two simulations — in this case, the neutrino mass loss. In the simulations with the other fiducial progenitors using Mode 1, the hydrodynamic shock ejects from the surface of the star "cleanly," where the packet of material moving outwards can be easily tracked and the leading and trailing edge of the shock are clear. In the case of the RSG, the tracking is not quite as easy.

The ambient material that the shock begins to sweep through when it ejects from the surface of the star causes the shock to expand, as seen in the density plot (Fig. B.2, bottom). While this is happening, the shock enters a higher velocity region (Fig. B.2, top). So, while the other fiducial progenitors were tracked using well defined velocity boundaries, the RSG had to be tracked using a large-enough negative gradient in the velocity (see Section 2.4.2). Although the script was successful in tracking the radii of the leading and trailing edges of the shock, the results of the mass and energy ejected from the RSG contain slightly more error due to the fact that the shock sweeps through some material outside of the star by the end of the simulation.

These test cases were important to run, because after making changes to the `FLASH` code and implementing all the changes described in Section 2.4, I had to make sure that `FLASH` still performed exactly as it did previously and

with respect to published work. So, these test cases are used to both compare my results with the ones published in Fernández et al. (2018) and as a mental check to make sure that if no neutrino mass-loss is included that these are indeed failed SN cases.

Appendix C

GR1D version 2

GR1D Version 2 was introduced in O'Connor (2015). The main change to the codes' capabilities relative to Version 1 is that neutrino transport is handled with a two-moment ("M1") multi-group scheme with an analytic closure for higher moments (Minerbo, 1978; Cardall et al., 2013). The critical additions for the neutrino transport calculations are the neutrino-matter interaction coefficients that describe the production, absorption, scattering, and annihilation of neutrinos. Neutrino source terms are applied in an operator-split way. Results from this new version of GR1D compare favourably to other state-of-the-art neutrino radiation-hydrodynamic supernova codes in spherical symmetry (O'Connor et al., 2018).

Initially, we completed more than half the simulations of the progenitors listed in Table 3.1 with GR1D version 2. For each EOS, neutrino emissivities, absorption and scattering opacities were generated using the NuLib[1] code (O'Connor, 2015) with default settings, which included rate contributions from Oda et al. (1994), Langanke and Martínez-Pinedo (2000), Langanke et al. (2003), and Sullivan et al. (2016). For neutrino transport, we evolved ν_e, $\bar{\nu}_e$, and a composite of heavy lepton neutrinos (ν_x), using 18 energy groups

[1] Available at nulib.org

of widths that increase at a constant ratio $\simeq 1.24$, with the lowest two bins having equal widths 2 MeV, spanning the energy range $[0, 311]$ MeV. Other parameters were identical to those used in the BH-forming progenitor described in O'Connor (2015) (commit `96aa353` in the public repository).

Simulations were initially run using an explicit treatment of energy coupling between groups. Once BH formation was approached, this treatment failed, and we (1) switched to implicit energy coupling between groups and (2) suitably reduced the Courant condition as recommended in O'Connor (2015). Unfortunately, even after applying the following fixes, the simulations never formed a BH due to convergence problems. That is not to say that the progenitors would not form BHs, we confirmed with Version 1 that they did, but that the Version 2 simulations were never able to be taken to their full extent of the $\delta M_{\rm G}$ difference.

It was after this that we decided to use `GR1D` Version 1, but for completeness, I present a quantitative comparison of the neutrino mass-loss between both versions of `GR1D` in Fig. C.1. This is done to obtain a reasonable estimate of the error introduced by using Version 1 over Version 2 of `GR1D` for our neutrino mass-loss evolution. I calculate the difference of the gravitational mass lost $\delta \mathrm{M}_G$ between the two versions in the following way:

$$\%_{\rm diff} = \left(\frac{\delta \mathrm{M}_{\rm G,v1} - \delta \mathrm{M}_{\rm G,v2}}{\delta \mathrm{M}_{\rm G,v1}} \right) \times 100\% \ , \tag{C.1}$$

where $\delta \mathrm{M}_{\rm v1}$ and $\delta \mathrm{M}_{\rm v2}$ correspond to the amount of gravitational mass lost in Version 1 and Version 2 of `GR1D` respectively. The gravitational mass lost is evaluated at $\mathrm{t}_{\rm end,v2}$ for both $\delta \mathrm{M}_{\rm G,v1}$ and $\delta \mathrm{M}_{\rm G,v2}$. The `GR1D` Version 2 simulations could not be evolved to the same $t_{\rm end}$ as Version 1, so the amount of gravitational mass lost is evaluated at the same elapsed time.

In Fig. C.1, we plot the gravitational mass lost with respect to time for all three fiducial progenitors, all three EOSs used, and both `GR1D` Version 1 and 2. The most obvious result is that all of the simulations from Version 2 stop at

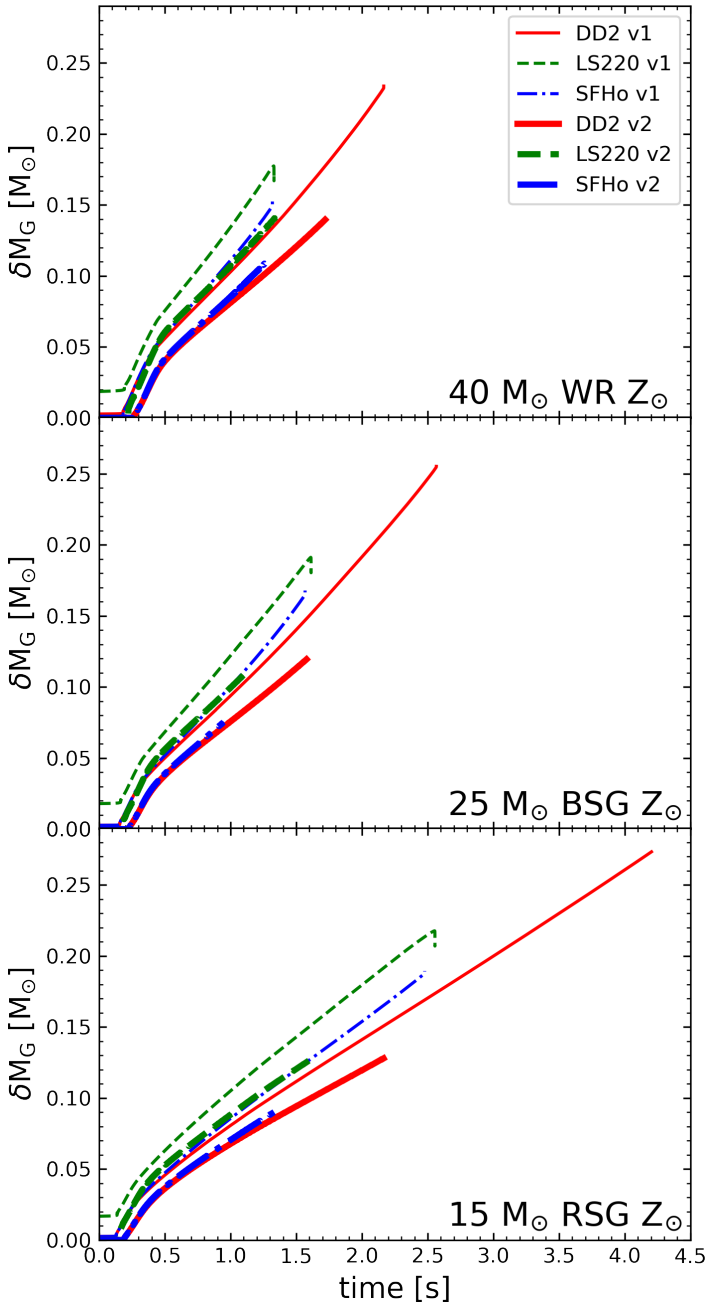

Figure C.1: Change in gravitational mass lost through neutrino mass-loss over time for `GR1D` version 1 (thin lines) and version 2 (thick lines) for all three fiducial progenitors and with all EOSs (DD2 – solid red lines; LS220 – dashed green lines; SFHo – dashed dotted blue lines).

an earlier time than those of Version 1, most clearly seen with the DD2 EOS. Also, as we know from Table 3.1, all the simulations from Version 1, except for the 15 $M_\odot$ RSG with the DD2 EOS, form a BH by the end of $t_{\rm end,v1}$, while none of the simulations from Version 2 form a BH.

When we compare the quantitative results of the amount of gravitational mass lost δM_G for the same elapsed time, on average, the `GR1D` version 2 simulations are all less than Version 1 — $\sim 16\%$ for RSGs, $\sim 19\%$ for BSGs, $\sim 20\%$ for WRs, or an average of $\sim 19\%$ overall across all simulations. So, for the purposes of quantifying the error on the neutrino mass-loss in our simulations, we can approximate them at $\sim 20\%$ to first order.

One last comparison we do is with the S40 progenitor and the LS220 EOS. We obtain a time (post-bounce) to BH formation of 0.53s (0.51s), a maximum PNS baryonic mass 2.45 $M_\odot$ (2.38 $M_\odot$), and a maximum PNS gravitational mass 2.31 $M_\odot$ (2.26 $M_\odot$) with the leakage (M1) version of GR1D. These masses are the same as those reported in O'Connor (2015), with BH formation times that differ by less than 10%. These results are also consistent (within $\sim 10\%$) with the 1D results of Pan et al. (2018) for the s40 progenitor using the LS220 EOS.

Appendix D

Low-resolution results

We report all our low-resolution runs for completeness in Table D.1. The resolution of these results is $\Delta r/r = 0.45\%$, the same as the highest resolution used in F18. While most of the results are very similar, the biggest differences between the results reported in Table 3.1 and Table D.1 are with the WR models. The effect of resolution on the results is fully discussed in Section 3.4.

Table D.1: Table of hydrodynamic models from `GR1D` V. 1.03 and summary of low resolution ($\Delta r/r = 0.45\%$) results, the highest resolution used in F18. Columns from left to right show the model name, time to BH formation from the onset of core-collapse $t_{\rm bh}$, maximum gravitational mass lost to neutrinos $\delta M_{\rm G}(t_{\rm bh})$, maximum kinetic energy of the shock in `FLASH` $E^{\rm sim}_{\rm k,max}$, total mass ejected in `FLASH` $M_{\rm ej}$, and total energy of ejecta $E_{\rm ej}$. The special model "W40S1.7" has $r_{\rm in} = 2 \times 10^7\,$cm, instead of the default $r_{\rm in} = 2 \times 10^8\,$cm used for *interpolation* mode.

Model	$t_{\rm bh}$ (s)	$\delta M_{\rm G}$ ($M_\odot$)	$E^{\rm sim}_{\rm k,max}$ (10^{47} erg)	$M_{\rm ej}$ ($M_\odot$)	$E_{\rm ej}$ (10^{47} erg)
R15S1	2.475	0.188	2.04	2.09	-0.206
R15S2			1.97	2.05	-0.215
R15S3			0.63	0.84	-0.246
R15L1	2.553	0.218	2.47	2.46	-0.089
R15D1	>4.204	>0.273	4.04	3.64	0.793
S20S1	2.037	0.170	0.66	0.68	-0.311
				$M_{\rm ej}$ (10^{-2} $M_\odot$)	
B25S1	1.5673	0.1645	2.15	2.73	0.440
B25S2			2.14	2.74	0.447
B25S3			<0.01	0.002	<-0.001
B25L1	1.6131	0.1905	2.54	3.14	0.593
B25D1	2.5664	0.2542	5.48	5.63	2.21
Y22S1	0.8117	0.1326	0.57	4.51	-0.006
Y25S1	1.6957	0.1367	1.81	7.17	-0.041
				$M_{\rm ej}$ (10^{-4} $M_\odot$)	
W40S1	1.3187	0.1489	1.27	1.21	0.054
W40S1.7			1.58	1.68	0.078
W40S2			1.25	1.18	0.053
W40S3			0.01	0	0
W40L1	1.3311	0.1767	1.61	1.72	0.079
W40D1	2.1661	0.2317	3.85	6.09	0.303
S40S1	0.8493	0.1250	0.13	1.67	-0.001
W50S1	0.7605	0.1202	0.48	0.45	0.016
B80S1	0.5034	0.0714	0.09	0	0